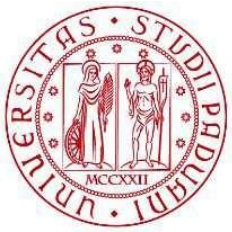

UNIVERSITÀ DEGLI STUDI DI PADOVA

UNIVERSITA' DEGLI STUDI DI PADOVA

DEPARTMENT OF

PHARMACEUTICAL AND

PHARMACOLOGICAL SCIENCES

Master thesis

Development of Anti-PD-L1 Immunoliposomes for Antitumor Drug delivery against skin cancer

Corrector: *Prof. Gianfranco Pasut*

Co-Corrector: *Maria Natalia Calienni, phD*

***Student**: Nastaran Chakhmaghi*

Academic Year 2024/2025

TABLE OF CONTENTS

ABBREVIATIONS

ATZ	Atezolizumab
CAN	acetonitrile
ATP	adenosine Triphosphate
AMP	adenosine Monophosphate
BCC	bsal cell carcinoma
BCA	bicinchoninic acid
$BaCl_2$	barium chloride
CV	crystal violet
C	constant
$CuSO_4$	copper (II) sulfate
DLS	dynamic Light Scattering
DSPE	1,2-distearoyl-sn-glycero-3-phosphoethanolamine
DMSO	dimethyl sulfoxide
DMEM	Dulbecco's Modified Eagle Medium
dsFv	disulfide-stabilized Fv
dH	Hydrodynamic diameter
EMEM	Eagle's Minimum Essential Medium
EDTA	ethylenediaminetetraacetic acid
EMA	European Medicines Agency
EPR	enhanced permeability and retention
EE%	Encapsulation efficiency
ε	Molar attenuation coefficient
FPLC	fast protein liquid chromatography
Fab	fragment antigen-binding
Fab`	fragment antigen-binding prime
Fc	fragment crystallizable
Fv	variable fragment
FBS	Fetal bovine serum
FDA	Food and Drug Administration
GLB	gel loading buffer
G	grams
HSPC	hydrogenated soybean phosphatidylcholine
Hh	Hedgehog signaling pathway
kDa	Kilodalton
KI	potassium Iodide
LUV	large unilamellar vesicles
LC	loading capacity
L	liters
MSC	melanoma skin cancer
MLV	multilamellar vesicles
MUV	medium unilamellar vesicles

MPS	mononuclear phagocyte system
MeOH	Methanol
m-PEG5kDa-DSPE	methoxy-polyethylene glycol-distearoyl phosphatidylethanolamine
mal-PEG5kDa-DSPE	maleimide-polyethylene glycol-distearoyl phosphatidylethanolamine
M	Molarity
MW	Molecular weight
NMSC	Non-melanoma skin cancer
OLV	Oligolamellar vesicles
pH	-log[H+]
Ptch	Patched
PD-L1	programmed death-ligand 1
PD-1	programmed cell death protein-1
PC	phosphatidylcholine
PBS	phosphate buffer solution
PEG	polyethylene glycol
RES	reticuloendothelial system
RP-HPLC	reverse-phase high-performance liquid chromatography
SC	stratum corneum
SCC	squamous cell carcinoma
SMO	smoothened
SUV	small unilamellar vesicles
scFv	Single-chain variable fragment
SPC	Soybean phosphatidylcholine
SEC	size exclusion chromatography
SDS-PAGE	sodium dodecyl sulfate-polyacrylamide gel electrophoresis
SL	Stealth liposome
SIL	Stealth immuno liposome
TFH	thin-film hydration
TFA	trifluoroacetic acid
TEM	transmission Electron Microscopy
UV-Vis	Ultraviolet-visible
UV-radiation	Ultraviolet radiation
ULV	Unilamellar vesicles
V	variable
v/v	volume/volume
w/w	weight/weight
λ	wavelength

ABSTRACT

Skin cancer, including melanoma and non-melanoma types, is among the most prevalent malignancies worldwide. Basal cell carcinoma (BCC) is the most common form of non-melanoma skin cancers, while melanoma remains the most aggressive subtype. Both cancers are characterized by the overexpression of programmed death-ligand 1 (PD-L1), an immune checkpoint protein enabling tumor immune evasion. On the other hand the aberrant activation of the Hedgehog (Hh) signaling pathway, promoting unchecked cellular proliferation. Targeting these two pathways simultaneously offers a promising strategy for improving therapeutic outcomes.

In this study, it was developed a dual-functional immunoliposome-based drug delivery system incorporating Vismodegib drug, a small-molecule inhibitor of the Hedgehog (Hh) signaling pathway, and the Fab' fragment of Atezolizumab, an antibody targeting PD-L1. Vismodegib was encapsulated within the liposomal bilayer to inhibit tumor growth, while the Fab' was conjugated to the liposome surface to enhance immune activation and tumor-specificity delivery.

After preparing various formulations, an optimal targeted formulation was achieved by conjugating the Fab' fragment of Atezolizumab to the surface of the liposome. Physico-chemical characterization of the immunoliposomes, including dynamic light scattering (DLS), zeta potential measurements, transmission electron microscopy (TEM), reverse-phase high-performance liquid chromatography (RP-HPLC), and SDS-PAGE, confirmed its suitability as a delivery system.

Cytotoxicity was assessed using two cell lines: HaCaT (human keratinocytes) and SK-Mel-28 (human melanoma), employing two different tests, crystal violet and ATP-lite. The results showed that the targeted formulation performed similarly to the free drug against tumor cells and demonstrated enhanced efficacy compared to the non-targeted formulation. Additionally, encapsulating Vismodegib into immunoliposomes reduced its cytotoxicity in non-tumor cells. However, further replications are needed to validate the efficacy of this system.

Therefore, an optimal formulation for delivering Vismodegib into PD-L1-targeted liposomes was successfully obtained and characterized. Preliminary *in vitro* results suggest its potential for skin cancer treatment, providing a basis for the further development of innovative invasive therapies.

1. AIM

The primary goal of this project was to design and optimize an advanced immunoliposome-based drug delivery system for the treatment of skin cancers, particularly basal cell carcinoma (BCC) and melanoma. These cancers are often associated with the dysregulation of critical biological pathways, such as the Hedgehog (Hh) signaling pathway, and the overexpression of immune checkpoint proteins like programmed death-ligand 1 (PD-L1), which contribute to uncontrolled tumor growth and immune evasion. The aim was to develop a dual-functional therapeutic platform that combines molecularly targeted therapy with immune modulation to improve cancer treatment outcomes.

The first objective was to formulate liposomes capable of efficiently incorporating Vismodegib, a hydrophobic small-molecule inhibitor that targets the Hh pathway. Given that the Hh pathway is a key driver of unregulated cell proliferation in BCC and melanoma, Vismodegib's ability to disrupt this signaling pathway makes it a significant therapeutic agent. The liposome formulation was optimized to ensure sufficient bilayer capacity and stability for encapsulating Vismodegib, which is hydrophobic and needs space within the bilayer for effective incorporation.

The second objective was to conjugate the Fab' fragment of Atezolizumab, an antibody targeting the PD-L1/PD-1 immune checkpoint, to the surface of the liposomes, transforming them into immunoliposomes. The Fab' fragment of Atezolizumab blocks the interaction between PD-L1 and PD-1, which is often overexpressed on cancer cells, thereby restoring immune system function and enhancing T-cell-mediated tumor cell destruction. This modification was aimed at addressing the immune evasion mechanisms utilized by skin cancers like BCC and melanoma.

The effectiveness of the developed system, VISMO-SIL, was evaluated through *in vitro* cytotoxicity assays in two cell lines: SK-Mel-28, a melanoma cell line, and HaCaT, an immortalized keratinocyte cell line, to assess differential effects between tumor and non-tumor cells.

2. INTRODUCTION

2.1. Cancer

Cancer stands out as the second leading cause of death worldwide, and its prevalence continues to grow rapidly. In the United States alone, approximately 1,665,540 individuals were diagnosed with cancer, and it was responsible for 585,720 deaths by 2014 (1). Therefore, cancer is considered a severe global health issue, impacting all human societies.

A critical challenge in cancer diagnosis and treatment is its complexity and variability (2). Cancer is a disease characterized by the uncontrollable growth of cells and their potential to spread to other parts of the body. Normally, cells grow and divide to form new cells as needed for the body. When cells grow old or become damaged, they typically die, and new cells take their place. However, sometimes this normal process does not occur. Instead, abnormal or damaged cells grow and divide when they shouldn't, potentially forming clusters of tissue known as tumors (Figure 1)(3).

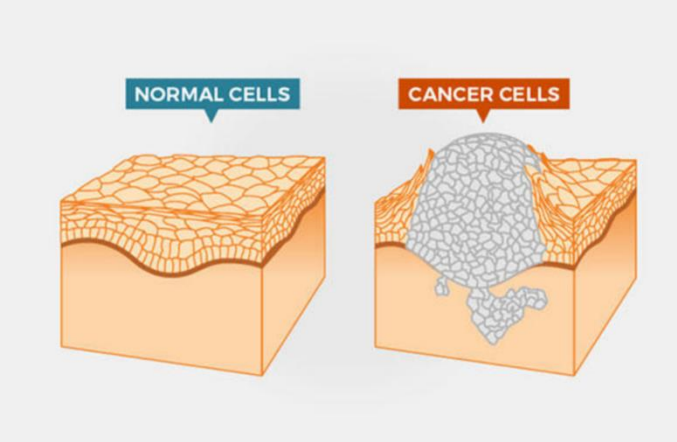

Figure 1: Cancer is a disease caused when cells divide uncontrollably and spread into surrounding tissues (4).

2.1.1. Cancer types

Tumors are classified into two groups: cancerous (malignant) and non-cancerous (benign)(4). Malignant tumors have aggressive growth and invade surrounding tissues and can spread to distant parts of the body through a process called metastasis. This spread allows malignant cells to form new tumors in other areas. Many cancers result in the formation of solid tumors, although certain types, such as blood cancers like leukemia, do not typically form solid masses.

Non-cancerous tumors, in contrast, do not invade nearby tissues or spread to other parts of the body. When removed, benign tumors usually do not grow back. This key distinction separates them from malignant tumors, which may recur after treatment.

2.1.2. Metastasis

When cancer spreads from its original site to another part of the body, it is referred to as metastatic cancer, and the process of spreading is called metastasis (Figure 2). Metastatic cancer retains the name and type of the original cancer. For example, if breast cancer spreads to the lungs, it is called metastatic breast cancer, not lung cancer. Under a microscope, metastatic cancer cells often resemble the cells of primary cancer and typically share similar molecular characteristics, such as specific chromosomal changes (4).

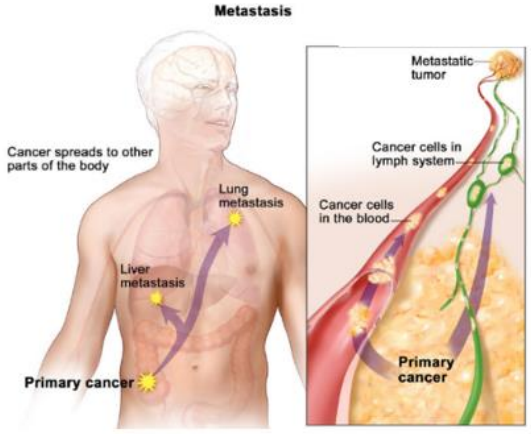

Figure 2: In metastasis, cancer cells break away from where they first formed (4).

In some cases, treatments for metastatic cancer can extend survival, while in others, the primary goal is to control cancer growth or relieve symptoms. Metastatic tumors can severely interfere with essential bodily functions, and most cancer-related deaths are due to metastatic disease (5).

2.2. Skin Cancer

The skin acts as a vital barrier, protecting the body from environmental threats while regulating water, ion, and nutrient exchange. It maintains homeostasis and supports critical functions, including temperature regulation, sensory reception, and hormone synthesis. Human skin consists of three primary layers: the epidermis, which provides a protective barrier (6); the dermis, which supports structural integrity and thermoregulation (7); and the hypodermis, which stores energy and provides insulation (8).

Skin cancer is one of the most prevalent types of cancer in the present decade (9). As the skin is the body's largest organ, the point of considering skin cancer as the most common type of cancer among humans is understandable (10). This cancer is classified into two main categories, non-melanoma skin cancer (NMSC) and melanoma skin cancer (MSC)(11). Among NMSC, the most common types are basal cell carcinoma (BCC) and squamous cell carcinoma (SCC), both of which originate from keratinocytes in the viable epidermis. Additionally, it is important to note that areas of the body exposed to the sun, such as the head and neck, are often the sites of skin malignancies, which can lead to serious complications during diagnosis and treatment. Treatment options include radiation, immunotherapy, chemotherapy, cryotherapy, and surgical excision. Using sunscreen and practicing proper sun safety are crucial measures to prevent skin cancer (12). Among all the different types of skin cancer, the three most common ones—BCC, SCC, and melanoma—originate in the viable epidermis (Figure 3)(13).

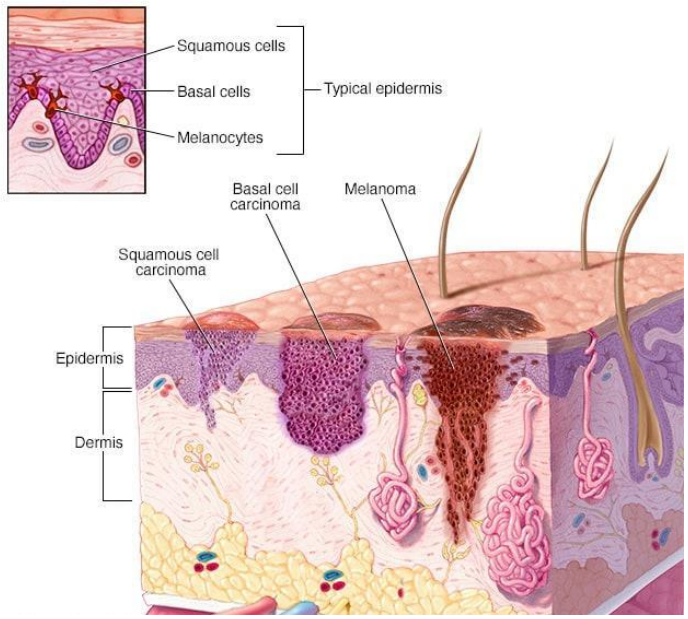

Figure 3: The image shows basal cell carcinoma, squamous cell carcinoma, and melanoma, the most common types of skin cancer (13)**.**

2.2.1 Basal cell carcinoma

Despite the fact that NMSC is more common than MSC, a total of 3.5 million cases of NMSC are diagnosed each year (14). Additionally, the incidence of NMSC has been increasing globally by 3–8% annually since 1960. Among NMSC cases, 80% are BCC, which is rising at a rate of 10% per year (15). It originates from the basal cells of the epidermis and primarily affects areas of the body exposed to sunlight. About 80% of cases occur on the head, with half of them affecting the skin of the cheeks and nose. BCC grows slowly and, if detected early, rarely metastasizes. BCCs are typically removed through surgery or desiccation, if possible, or treated with radiation therapy. However, because they often appear in areas that are chronically exposed to the sun, the physical and emotional impact of excision is significant for patients (16). Additionally, when these tumors advance, the chances of achieving effective treatment decrease. BCC can cause local destruction, severe deformity, and spread to nearby areas, compromising sensory organs, as well as metastasize to other regions of the body and become fatal.

2.2.2. Squamous Cell Carcinoma

SCC is another common type of skin cancer that typically develops in sun-exposed areas of the skin. It often appears as a well-defined, red, scaling, thickened bump, which can ulcerate and

bleed if left untreated (17). SCC is a non-invasive lesion that does not spread to nearby tissues because it is superficial, and the risk of it transforming into invasive SCC is low, around 3-4%. Although SCC usually grows slowly, it may spread more rapidly in individuals with weakened immune systems. Like BCC, early detection and treatment of SCC generally lead to positive outcomes (18).

2.2.3 Melanoma

Melanoma is the most aggressive form of skin cancer and arises from melanocytes, the cells responsible for producing skin pigment. Despite its less frequency than BCC and SCC, melanoma poses a greater risk of metastasizing to other parts of the body. Early detection is crucial, as symptoms may include changes in the size, shape, color, or elevation of moles (19). Melanoma is now regarded as the fifth most common cancer in men and the sixth most common cancer in women in the United States, where the incidence of malignant melanoma from 1973 to 2002 increased by 270% (20).

The incidence of melanoma in Italy is equal to 5-7 cases per 100,000 inhabitants per year even though Mediterranean populations are at low risk for the development of this tumor (21). Melanoma is particularly prevalent among younger individuals, especially those aged 25 to 29 (17).

2.3. Skin cancer treatments

Conventional treatments for skin cancer, such as surgery, chemotherapy, and radiotherapy, have long been employed as primary interventions. These methods are effective but often non-specific, leading to damage to surrounding healthy tissues and significant side effects (22). Advanced techniques like photodynamic therapy and photothermal therapy improve on these by selectively targeting tumor cells while minimizing harm to adjacent tissues. However, they also face limitations such as reduced penetration and resistance in deeper or aggressive tumor types (23).

Nanotechnology-based therapies are emerging as transformative alternatives, offering precise drug delivery through nanoparticles that can overcome physiological barriers and achieve targeted action. These approaches enhance drug efficacy while reducing toxicity. Nanoparticles enable site-specific delivery of chemotherapeutics, phototherapeutics, and they are often engineered to improve cellular uptake and retention in tumors (24).

While recent studies are focused more on the integration of nanotechnology with targeted therapies further enhances outcomes. For instance, nanoparticles can carry a combination of drugs or therapeutic agents, such as inhibitors of molecular targets or immune checkpoint proteins. This dual or multi-pronged approach maximizes anti-tumor effects by targeting cancer-specific pathways while minimizing off-target effects. Studies show that combining nanotechnology-driven delivery systems with targeted immunotherapies like checkpoint inhibitors amplifies tumor response and can overcome multidrug resistance (25). Thus, the synergy of nanotechnology and targeted therapies represents a promising paradigm for treating skin cancer, addressing the limitations of conventional methods and enhancing precision and efficacy in treatment.

2.4. Nanotechnology

Nanoparticles are drug delivery systems, created by using biodegradable materials like natural and synthetic polymers, lipids, or metals, with an average size smaller than 100 nm in one dimension. Small-size nanoparticles, which allow for easy uptake by cells, make them ideal for drug delivery. For therapeutic applications, drugs can either be integrated into the matrix of the particle or attached to the particle surface. Nanoparticles can be used in targeted drug delivery at the site of disease to enhance the uptake of poorly soluble drugs, the targeting of drugs to a specific site, and drug bioavailability. Various colloidal drug delivery systems like liposomes and micelles have been extensively studied for their potential in cancer therapy. Drug delivery systems are effective due to their tiny size, reduced drug toxicity, regulated drug release, and alterations in drug pharmacokinetics and biological distribution (26).

2.4.1. Liposomes

Liposomes, as one of the most common nanoparticles, are lipid-based, self-assembling vesicles that are widely used in medication administration because of their special structural and functional characteristics. They consist of one or more phospholipid bilayers that enclose an aqueous compartment, allowing them to encapsulate both hydrophilic and hydrophobic drugs (27). In the presence of aqueous media, they self-assemble, forming highly ordered structures called bilayer sheets, which are thermodynamically unfavorable and tend to close, forming spherical multilamellar vehicles. This feature is the discriminant factor between liposomes and micelles (Figure 4), which instead are made of wedge-shaped phospholipids bearing only one acyl tail and upon self-assembling they form spherical structures with a filled hydrophobic core and a hydrophilic surface (28). So, the hydrophilic drugs will incorporate to the aqueous core

and the hydrophobic drugs, as was done in this project, in the bilayer of the liposome (Figure 5).

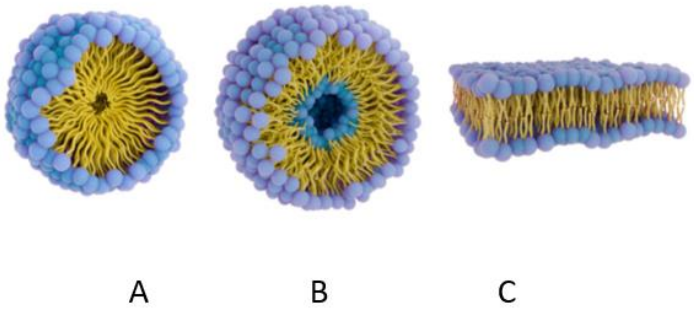

Figure 4: schematic representation of a micelle (A), a liposome (B), and a lipid bilayer sheet (C)(29)**.**

2.4.2. Main components of liposomes

The major components of liposomes are phospholipids and cholesterol. The chemical properties of these lipids control liposome behavior. Phospholipids, such as phosphatidylcholine (PC), form the bilayer structure of liposomes, with hydrophobic tails oriented inward and hydrophilic heads facing outward, creating a stable environment for drug incorporation. One of the most favored PC for liposome synthesis are synthetic PC and natural PC, found in sources like eggs, soy, and other natural sources. Additionally, functional PC, such as 1,2-distearoyl-sn-glycero-3-phosphoethanolamine (DSPE), are used to conjugate other polymers, such as polyethylene glycol (PEG), to optimize liposome function. PEG is a frequently used component, typically included to enhance blood circulation time (30). Another component often added to the liposomal formulation to stabilize the bilayer is cholesterol, which provides the liposome with fluidity, elasticity, permeability, and stability. The most important advantages of liposomes are features like increasing the efficacy and therapeutic index of the drug, reducing the toxicity of the drug and coupling with site-specific ligands to achieve active targeting while the significant disadvantages are related to their blood stream short half-life and low level of solubility (31).

2.4.3. Liposome classification

Liposomes are generally classified based on their structural characteristics into two main types: unilamellar vesicles (ULV) and multilamellar vesicles (MLV). ULV of a single lipid bilayer can be further categorized according to their size. Small unilamellar vesicles (SUV) are typically less than 100 nm in diameter, medium unilamellar vesicles (MUV) range from 100 nm to 250

nm, and large unilamellar vesicles (LUV) are larger than 250 nm. On the other hand, MLV contains multiple lipid bilayers, which increase their internal volume and enhances their capacity for encapsulating larger quantities of substances. Oligolamellar vesicles (OLV), while like MLVs, contain fewer bilayers. The structural differences between these types of liposomes provide various advantages depending on their intended use, such as controlled drug delivery or targeted treatment (Figure 5)(27).

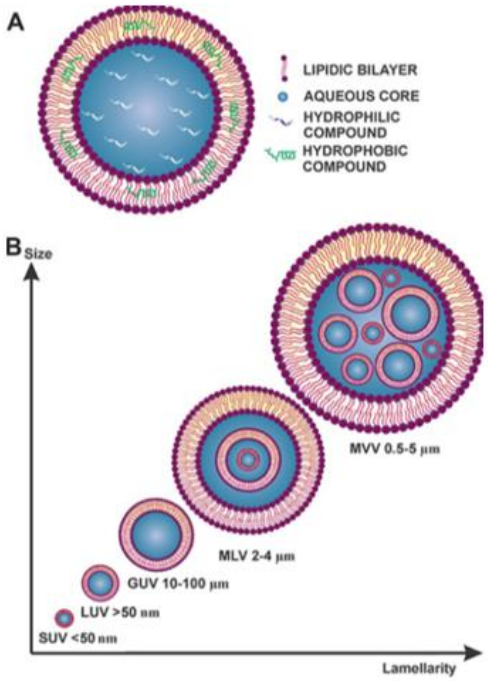

Figure 5: Schematic representation of a liposome (A), Classification of liposome (B)(32).

2.4.4. Liposome preparation methods

There are various conventional methods to prepare liposomes. The primary goals of liposome nano formulation methods are to achieve monodisperse particles with a narrow size distribution, the desired lamellarity, efficient drug encapsulation, and long-term colloidal stability. Conventional methods involve dissolving lipids in a volatile organic solvent, followed by mixing with an aqueous phase. However, the organic solvent can alter the chemical properties of the active compounds, affect stability, or increase toxicity in the resulting formulation. The conventional methods to prepare liposomes involve these main features mentioned below (33):

- Dissolution of lipids in an organic solvent.
- Drying down the resultant lipidic solution from the organic solvent.
- Hydrating the lipid with aqueous media (followed by agitation/stirring).
- Downsizing (and/or change in lamellarity).
- Post-formation processing (purification, sterilization).
- Characterization of the final nano formulation.

Among all the present different methods for liposome preparation, the liposomes of this project were prepared with the thin-film hydration (TFH) Method (Bangham Method) that is explained below:

2.4.4.1. Thin-Film Hydration Method (Bangham Method)

This method is the method that was used in this project to prepare the liposome formulation. The TFH technique (the so-called Bangham method) is the oldest, most common method used for the preparation of MLVs (Figure 6)(34). To make a homogeneous mixture, the main phospholipid ingredients are dissolved in an organic solvent (such as dichloromethane, chloroform, ethanol, or a chloroform-methanol mixture). Subsequently, the organic solvent is removed by evaporation under the vacuum pump of the rotary evaporator at a temperature of 30 °C. Then a dry thin lipid film is formed. In the next step, the hydration of the film must be done through the vortex mixing or rotating with rotary evaporator instrument under the suitable temperature for the lipid. The agitation helps detach the lipids' lamellae from the internal surface of the rounded bottom flask. Concerning the drug loading into liposome systems, lipophilic drugs can be dissolved with the phospholipids mixture before the thin film formation, while hydrophilic cargoes can be inserted within the hydration mediums and then incorporated (passively) into the liposome during the hydration process. The final step in the preparation of the hydrated liposome formulation involves extrusion through a polycarbonate membrane using an extruder. The device allows the use of membranes with varying pore sizes to ensure size and lamellarity uniformity of the liposomes. The formulation is sequentially extruded through membranes with pore sizes of 400 nm, 200 nm, and 100 nm, each for 10 passes. Subsequently, it is passed through a 50 nm membrane four times. This extrusion process serves to reduce the liposome size and improve their uniformity in both size and lamellarity, ensuring a more consistent and homogenous liposomal formulation.

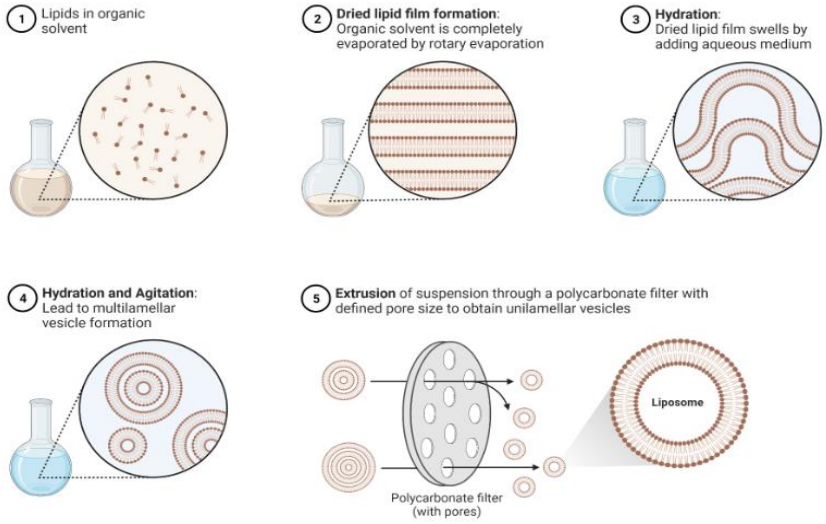

Figure 6: Thin film hydration steps.

2.4.5. Conventional Liposomes

First generation or conventional liposomes, as mentioned before, are small vesicles made of phospholipids like PC and cholesterol, forming a lipid bilayer structure which can encapsulate both hydrophilic and hydrophobic drugs (Figure 5)(35). Size and lamellarity are two factors that can be used to classify conventional liposomes. Various parameters, like encapsulation efficiency, drug release profile, physical stability during storage, and cell internalization capacity, are influenced by the size and quantity of bilayers (36). The method that is used to prepare liposomes affects the size and the number of bilayers of the liposome. The thin-film hydration method creates multilamellar vesicles, Other methods are used for preparing large unilamellar vesicles, and small unilamellar vesicles are generated by sonication or multiple extrusions through a polycarbonate membrane (37). The main advantage of these liposomes is their potential to be biocompatibile and ability to protect the incorporated drug from degradation, enabling a more improved drug delivery system (38).

First-generation liposomes faced significant challenges in stability and circulation within the body, as they were often rapidly cleared from the bloodstream by the mononuclear phagocyte system (MPS). This led to a short half-life and, consequently, limited therapeutic efficiency (39). A wide range of improvements in the formulation and preparation methods of liposomes were assessed, but despite all of them, first-generation liposomes still face challenges in achieving targeted delivery and prolonged circulation time in the bloodstream. To get beyond

these restrictions as much as possible, second-generation liposomes with surface modification possibilities are created.

2.4.6. Stealth liposomes

Stealth liposomes, a breakthrough in drug delivery systems, are designed to enhance the targeting and accumulation of therapeutic agents in tumor tissues while minimizing systemic toxicity (39). This design leverages the enhanced permeability and retention (EPR) effect, a phenomenon where the abnormal vasculature in tumors, characterized by large endothelial gaps and poor lymphatic drainage, allows nanoparticles like liposomes to preferentially accumulate in tumor tissues. PEGylation, the conjugation of PEG to the surface of liposomes, plays a pivotal role in their enhanced performance (Figure 7). The hydrophilic PEG layer prevents recognition by opsonin and the reticuloendothelial system (RES), protecting the liposomes from rapid clearance by organs such as the liver and spleen (40). This prolonged circulation time ensures that PEGylated liposomes remain in the bloodstream longer, increasing their chances of reaching tumor sites. Additionally, the PEG coating helps achieve an optimal particle size, reducing loss through renal filtration while facilitating efficient tumor targeting (41). Once accumulated in the tumor microenvironment, where drainage is poor, these liposomes create a local drug depot, gradually releasing their therapeutic payload directly at the site. This combination of EPR-based targeting and RES evasion makes stealth liposomes a highly effective strategy for cancer therapy, as demonstrated by FDA-approved formulations like Doxil®, DaunoXome®, and others that exploit these principles for enhanced drug delivery and therapeutic outcomes (42).

2.4.7. Targeted liposomes

Endocytosis or membrane fusion enables liposomes to deliver their incorporated drug inside the cell. A significant cell-specific uptake is achieved by active targeting liposomes, which enter targeted cells via receptor-mediated endocytosis. Conjugating the suitable targeting ligands, such as small molecules, aptamers, monoclonal antibodies and peptides on the surface of the liposomes manipulates the cell-type-specific uptake (43). Immunoliposomes are liposomes that are engineered by attaching specific antibodies or their fragments to their surface, enabling them to selectively target cells that overexpress certain antigens. These targeted liposomes can deliver therapeutic agents more precisely, reducing side effects and increasing efficacy. Immunoliposomes can be produced through the surface functionalization of liposomes, which involves covalently coupling modified PEG termini to monoclonal antibodies or their smaller

fragments, such as fragment antigen-binding (Fab') and single-chain variable fragments (scFv)(44). This surface modification allows the liposomes to recognize and bind to specific antigens on the target cells, enhancing their ability to deliver drugs directly to those cells (Figure7). Although immunoliposomes can treat autoimmune and degenerative diseases, inflammatory and cardiovascular diseases, and infectious pathologies, but are widely studied for cancer therapy (44).

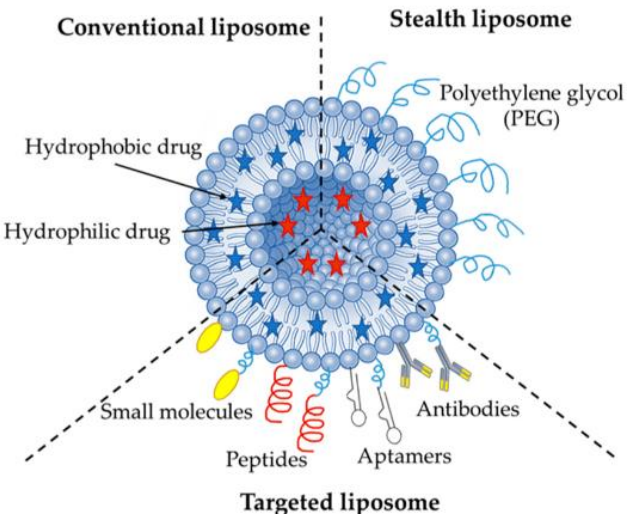

Figure 7: Schematic illustration of conventional, PEGylated/stealth, and ligand-targeted liposome (45).

2.5. Antibody

Nowadays, protein therapies are highly demanded. Protein drugs show significant effects at low concentrations with fewer side effects rather than small molecule drugs. Among protein drug therapies, antibodies play a key role in controlling different diseases such as cancer, infectious diseases, allergies, autoimmune diseases, and inflammation (46). Antibodies, also known as immunoglobulins, are specialized proteins that are present in both blood and tissue fluids. The immune system produces them to recognize and eliminate foreign things including poisons, pathogens (viruses, bacteria), and other dangerous agents. In Some cases, the potential side effects of antibodies are reduced due to their specificity and their ability to conjugate to another therapeutic entity for efficient delivery of that entity to the target site (47).

2.5.1. Antibody structure

Antibodies are Y-shaped molecules that consist of four protein chains held together by disulfide bonds (Figure 8). A disulfide bond is a covalent bond between the sulfhydryl groups of two cysteine amino acids. Antibodies contain two identical heavy (H, 50 kDa) and two identical light (L, 25 kDa) chains. Therefore, the total molecular weight is approximately 150 kDa. The variable (V) regions of both chains cover approximately the first 110 amino acids, forming the Fab regions, whereas the remaining sequences are constant (C) regions, forming fragment crystallizable (Fc) regions for effector recognition and binding. Immunoglobulins are classified into five major types: IgA, IgD, IgE, IgM, and IgG. The most abundant in human serum, accounting for 10-20% of plasma proteins, and widely used for therapeutic purposes are IgGs (46).

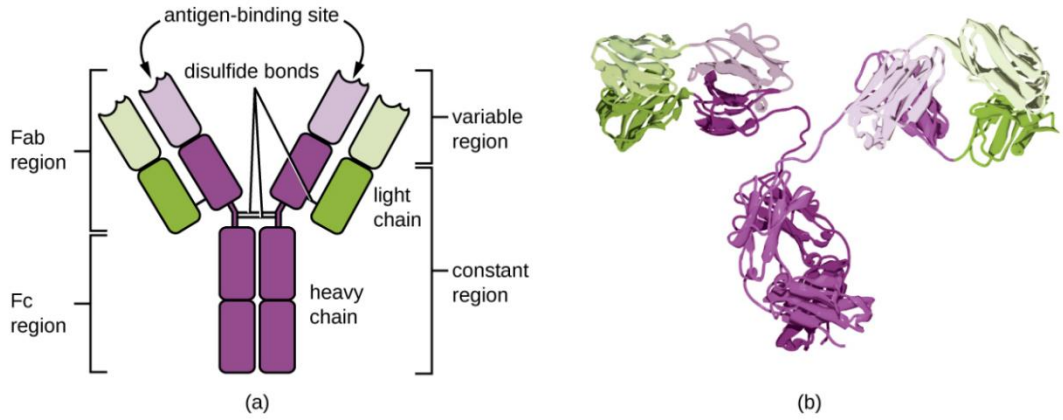

Figure 8: The typical four-chain structure of a generic antibody monomer(a), The corresponding three-dimensional structure of the antibody IgG(b).

2.5.2. Antibody fragments

Complete antibody structures like IgG are well-used in therapeutics, but smaller antibody fragments provide better advantages. The molecular size is the main difference: IgG is around 150 kDa, while fragments like Fabs are around 50 kDa, with some fragments being even smaller. More diffusion rate, more penetration rate into targeted tissues and tumors are the good results of their size reduction (48). Various enzymatic proteolysis helps to generate antibody fragments in the laboratories. For example, Papain makes two monovalent Fabs and one Fc per molecule of IgG by cleaving above the hinge disulfide bonds. Pepsin produces one bivalent

F(ab')$_2$ per IgG by cleaving below the hinge disulfides which can be further split into two Fab' molecules in the presence of a reducing agent (49). The next most explored types of antibody fragment include the variable fragment (Fv), disulfide-stabilized Fv (dsFv), and the single-chain variable fragment (scFv). These fragments contain the VH and VL domains, with dsFv stabilized by a disulfide bond and scFv linked by a short amino acid linker. The scFv, at about 28 kDa, is the smallest antibody fragment retaining native variable regions, offering advantages like low-cost prokaryotic expression and enhanced tissue penetration. However, these benefits come with trade-offs, including faster clearance and the absence of effector functions (Figure 9)(50).

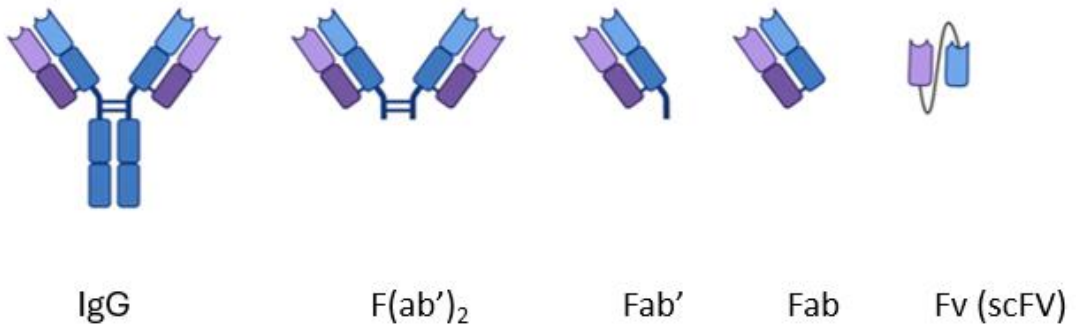

Figure 9: A full IgG antibody and common antigen binding fragments (50).

2.5.3. Tecentriq® (Atezolizumab)

Atezolizumab, marketed under the brand name Tecentriq®, is a monoclonal antibody used as an immune checkpoint inhibitor in cancer therapy (51). It functions by recognizing the protein known as programmed death-ligand 1 (PD-L1) that is overexpressed on the surface of some cancer cells. Certain cancer cells use a protein called PD-L1 to elude the immune system, preventing them from being discovered and eliminated. Atezolizumab, by attaching itself to PD-L1, stops it from interacting with T-cells' programmed cell death protein-1 (PD-1) receptor. The immune response against cancer cells is typically weakened by the suppression of T-cell activity caused by the PD-L1/PD-1 interaction. Atezolizumab restores the immune system's capacity to identify and combat cancer cells by preventing this interaction. By increasing T-cell activity, this PD-L1 inhibition strengthens the immune response against the tumor (52).

2.6. PD-1/PD-L1 signaling pathway

PD-1 and its ligand, PD-L1, constitute a pivotal immune checkpoint pathway involved in regulating T cell-mediated immune responses, particularly within the tumor microenvironment (53). PD-1, an inhibitory receptor expressed on activated T cells, binds to PD-L1, a ligand commonly overexpressed on tumor cells as well as certain antigen-presenting cells. This interaction delivers an inhibitory signal to T cells, leading to reduced cytokine production, impaired proliferation, and functional exhaustion. Under normal physiological conditions, the PD-1/PD-L1 axis plays an essential role in maintaining immune tolerance and preventing autoimmunity by limiting T cell activation in peripheral tissues (54).

However, many tumors exploit this pathway by upregulating PD-L1 expression, which suppresses T cell activity and enables immune evasion (55). This immune escape mechanism fosters an immunosuppressive microenvironment that supports tumor growth and metastasis. Targeting the PD-1/PD-L1 interaction with immune checkpoint inhibitors has emerged as a transformative approach in oncology, reactivating T cells to overcome immune tolerance and enabling robust anti-tumor responses. Therapies that block PD-1 or PD-L1, such as monoclonal antibodies, have shown significant efficacy across a broad spectrum of malignancies, including non-small cell lung cancer, melanoma, renal cell carcinoma, and urothelial carcinoma, thus highlighting the central role of the PD-1/PD-L1 pathway in cancer immunotherapy (56).

Studies indicate that PD-L1 overexpression occurs in approximately 62% of cutaneous melanoma cases (57), and the inhibition of the PD-1/PD-L1 pathway has shown significant therapeutic potential for this type of cancer. Similarly, PD-L1 overexpression in BCC has been reported to range from 22% to 89.9% (57), suggesting that targeting this pathway could also be a viable therapeutic option for BCC. This therapeutic approach effectively counters the immune escape mechanisms tumors use to evade immune detection. By blocking the PD-1/PD-L1 interaction, T cells are reactivated, leading to enhanced immune responses against the tumor (Figure 10)(58).

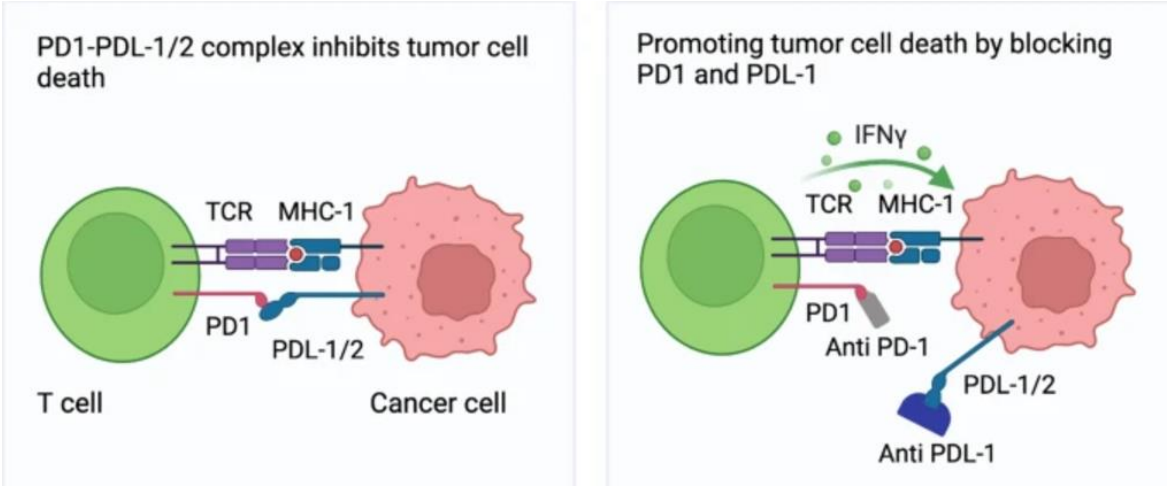

Figure 10: PD-1/PD-L1 blockade pathway(59).

2.7. Hedgehog signaling pathway

The Hedgehog (Hh) signaling pathway is a fundamental mechanism involved in embryonic development and tissue regeneration. Recent studies have highlighted its crucial role in the development and progression of various cancers, including skin cancer. This pathway works through several main parts. Hedgehog ligands (Sonic, Desert, and Indian Hedgehog) start the process by attaching to Patched (Ptch) receptors. Normally, Ptch receptors block the Smoothened (SMO) receptor from working (Figure 11). But when SMO is activated, it triggers a chain of events that leads to the activation of Gli transcription factors, which control genes involved in cell growth, survival, and differentiation. Dysregulation of the Hh signaling pathway is a significant driver of several skin cancers, particularly BCC. BCC, the most common form of skin cancer, is often caused by mutations in the PTCH1 or SMO genes, which result in constant activation of the Hh pathway and uncontrolled cell proliferation (60). Targeting this pathway has become a key therapeutic strategy for treating advanced BCC.

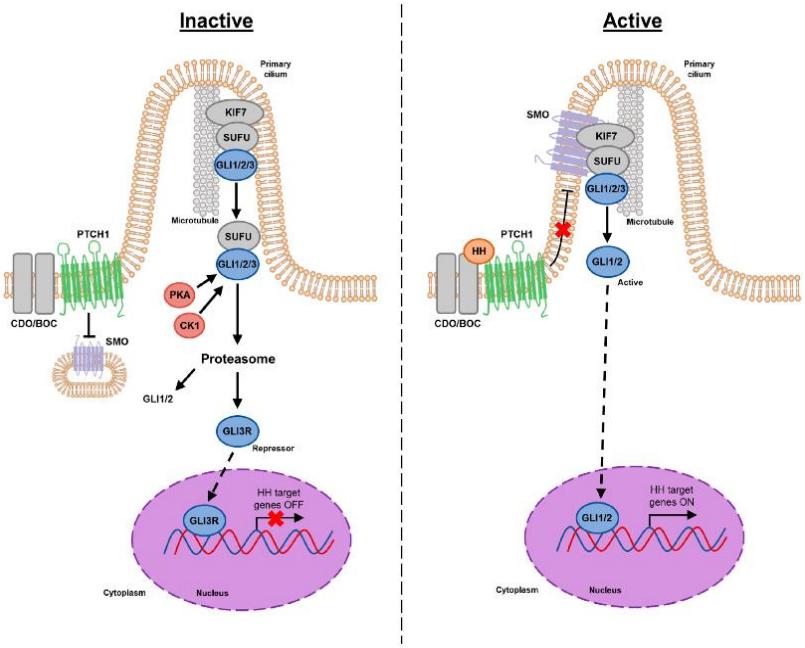

Figure 11: Overview of the canonical Hedgehog signaling pathway (61).

2.8. Vismodegib

In 2012, the FDA and in 2013, the European Medicines Agency (EMA) approved Vismodegib, 2- chloro- [4- chloro-3- (pyridin-2- yl) phenyl] -4-(methylsulfonyl) benzamide (Erivedge®) (Figure12), the first selective inhibitor of its class targeting the transmembrane protein SMO, which acts on the Hh signaling pathway (62). The common side effects include mild to moderate muscle spasms, alopecia, dysgeusia or ageusia, weight loss, fatigue, nausea, diarrhea, decreased appetite, constipation, arthralgia, amenorrhea, and vomiting (symptoms reported in the prospectus). Additionally, based on its mechanism of action, Vismodegib can cause embryonic or fetal death or serious congenital defects when administered to a pregnant woman (63). Despite these side effects, Vismodegib has shown high response rates and long-term efficacy in patients with advanced BCC. Although most BCCs are treated surgically, these lesions occasionally progress to a locally advanced state that cannot be treated by surgery or radiotherapy, recur after surgery, or, less frequently, spread to distant sites causing metastasis. Until 2012, there was no effective therapy for these locally advanced or metastatic BCC types and the therapeutic approach for these patients was exclusively conventional chemotherapy with limited benefits (64).

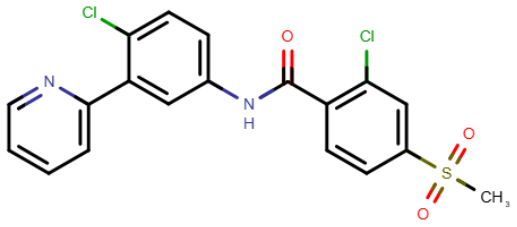

Figure 12: Vismodegib chemical structure.

2.9. Combined therapy

Despite the promise of therapies like Vismodegib, which inhibits the Hh signaling pathway, clinical observations have revealed that some patients develop resistance due to adaptive mutations in the SMO receptor (65). This resistance highlights the need for alternative treatment strategies. Consequently, combination therapies targeting multiple molecular pathways have gained attention as a potential solution to overcome resistance mechanisms. On July 30, 2020, the FDA approved the combination of Atezolizumab with Vemurafenib and Cobimetinib as a first-line treatment for unresectable melanoma, marking the first approved regimen that integrates both targeted therapy and immunotherapy(66).

This project investigates a combined therapy for cancers that overexpress PD-L1, focusing specifically on BCC and melanoma, both of which exhibit high levels of PD-L1 expression. The proposed therapy utilizes Atezolizumab Fab', an anti-PD-L1 antibody fragment, to target and inhibit the PD-L1 receptor. Additionally, Vismodegib, an inhibitor of the Hh signaling pathway, is incorporated into the drug delivery system to enhance therapeutic efficacy (Figure 13). This dual-target approach may offer a more effective treatment strategy, potentially reducing the risk of resistance and improving outcomes for patients with skin cancers that overexpress PD-L1 and present an overactivation of Hh. To enhance drug delivery, we utilize stealth immunoliposomes as drug delivery systems, which can improve the stability, targeting, and release of the therapeutic agents. The goal of this combination therapy is to provide a less invasive treatment option for patients with BCC and melanoma, potentially improving outcomes while minimizing side effects.

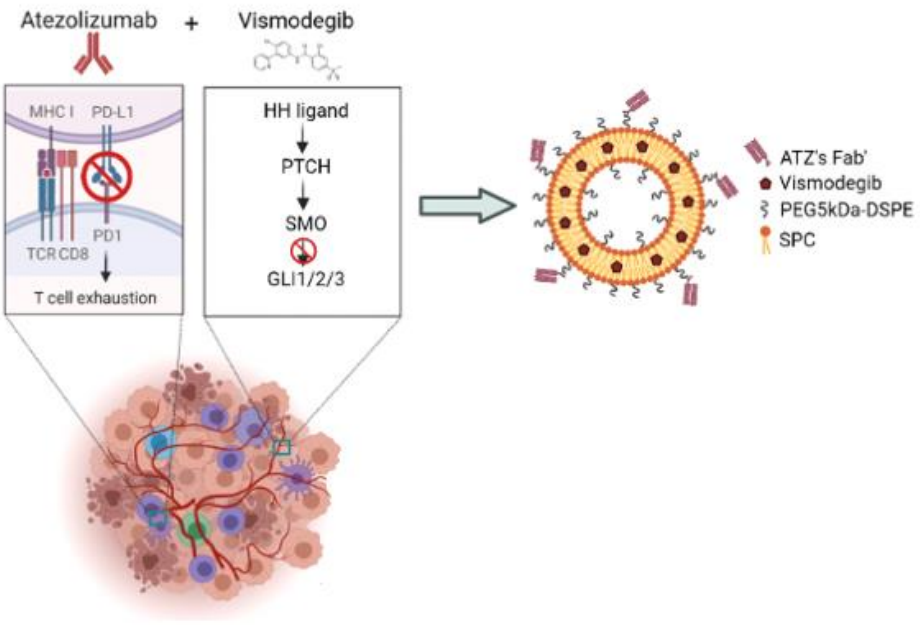

Figure 13: Project combined therapy strategy for skin cancer treatment.

ATZ`s Fab': Atezolizumab fragment antigen-binding

SPC: Soybean phosphatidylcholine

3. MATERIALS&METHODS

3.1. Materials

Chloroform, ethanol, methanol (MeOH), acetonitrile (ACN), dimethyl sulfoxide (DMSO), cholesterol, sodium chloride, potassium chloride, potassium phosphate monobasic, sodium acetate, disodium hydrogen phosphate dihydrate, ethylenediaminetetraacetic acid dihydrate,iron (III) chloride hexahydrate and ammonium thiocyanate, thioglycolic acid and coomassie brilliant blue R-250, Pepsin, trifluoroacetic acid (TFA), crystal violet (CV), bicinchoninic acid (BCA) kit for protein determination for 200-1000 µg/mL and QuantiPro BCA Assay (micro-BCA) kit for 0.5-30 µg/mL protein concentration, and ProteoSilver Plus Silver Stain kit were purchased from Sigma-Aldrich (St. Louis and Burlington, MA, USA). Ethanol, MeOH, ACN, and TFA were HPLC-grade. The aqueous solutions were prepared with Milli-Q grade water.

Hydrogenated soybean phosphatidylcholine (HSPC), methoxy-polyethylene glycol-distearoyl phosphatidylethanolamine (m-PEG_{5kDa}-DSPE), and maleimide-polyethylene glycol-distearoyl phosphatidylethanolamine (mal-PEG_{5kDa}-DSPE) were purchased from Nof Corporation (Tokyo, Japan).

Soybean phosphatidylcholine (SPC) was purchased from Lipoid (Ludwigshafen am Rhein, Germany).

Vismodegib was purchased from MedChemExpress (Princeton, NJ, USA).

Tecentriq® (Atezolizumab) and Herceptin® (Trastuzumab) were purchased from Roche (Basel, Switzerland).

Dulbecco's Modified Eagle Medium (DMEM), trypsin-EDTA (0.25 % in HBSS with phenol red), penicillin, streptomycin, glutamine, and fetal bovine serum (FBS) were purchased from Sial (Rome, Italy).

Eagle's Minimum Essential Medium (EMEM) medium, HACAT (T0020001) and SK-MEL-28 (C0020001) cell lines were purchased from AddexBio (San Diego, CA, USA).

Cysteamine was purchased from Honeywell Fluka (Charlotte, NC, US).

The filters of cellulose acetate of 0.22 μm and 0.45 μm used to filtrate the aqueous solutions were purchased from Sarstedt (Nümbrecht, Germany).

The proteins were concentrated using both Vivaspin® 500 PES membrane 30 kDa MWCO from Sartorius Stedim Lab (Stonehouse, UK), for small sample volumes, and Amicon®Ultra-0.5 30 kDa MWCO from Thermo Fisher Scientific (Waltham, MA, USA) for greater volumes.

The pH measurements were carried out with a pH-meter mod. 82 Radiometer (Copenhagen, Denmark) with Metrohm 794 Basic Titrino electrode (Herisau. Switzerland).

Liposomes were extruded using a LipoFast Basic extruder purchased from Avestin Europe GmbH (Manheim, Germany) through Whatman Nuclepore Track-Etch membranes made of polycarbonate (400-200-100-50 nm pore size) purchased from GE Healthcare Life sciences (Düsseldorf. Germany) and filter supports (10 mm pore size) were purchased from Avanti Polar Lipids (Hamburg, Germany).

GraphPad Prism 8.0.1 software was used to illustrate the graphs.

3.2. Methods

3.2.1. Stealth liposome preparation

Stealth liposomes were prepared using the TLE technique. The components (HSPC/SPC, m-PEG_{5kDa}-DSPE/mal-PEG_{5kDa}-DSPE, vismodegib, and cholesterol) were dissolved in 2 mL of $CHCl_3$: CH_3OH at a ratio of 3:1 v/v in a round-bottom flask (Table 1, 2). Subsequently, chloroform and methanol were removed via rotary evaporation, first, for 10 minutes under 200 mbar pressure, forming a lipid film, then followed by drying under vacuum for 60 minutes under 70 mbar pressure. Using a vortex, the lipid film was then hydrated with 2 ml of PBS 1 (pH 7.4). The obtained liposomal suspension was extruded, passing it ten times through polycarbonate filters with decreasing pore sizes 400-200-100 nm and 4 times with 50nm at 65 °C.

Several liposome formulations were prepared and tested to identify the optimal formulation concerning stability, drug encapsulation efficiency, and retention within the lipid bilayer, as shown in Table 1. This iterative process involved varying parameters such as lipid composition, PEGylation, and cholesterol content, with some formulations containing cholesterol and others not. These variations allowed for a systematic assessment of each component's impact on the overall performance of the liposomes as drug delivery vehicles. Based on the formulation assessments, “Formulation 8” was identified as the optimal formulation to continue with the characterization of the Stealth Immunoliposomes (Table 2).

Formulation	Lipid composition	Cholesterol	m-PEG_{5kDa}-DSPE	Vismodegib
Formulation 1	HSPC 16	8	1	1
Formulation 2	SPC 16	8	1	1
Formulation 3	SPC 16	5	1	1
Formulation 4	SPC 16	5	1	0.5
Formulation 5	SPC 16	0	1	1
Formulation 6	SPC 16	0	1	0.5
Formulation 7	SPC 16	0	1	0.25
Formulation 8	SPC 16	0	1	0.4
Formulation 9	SPC 16	0	1	0.35

Table 1: Different formulations composition of stealth liposomes based on molar ratio.

Components	Molecular weight (MW)	Mass
SPC	775 Da	0.030 gr
$mPEG_{5kDa}$-DSPE	6116 Da	0.01461 gr
Vismodegib	421 Da	0.003 gr

Table 2: Molecular weight and mass of liposome components for preparing 2 ml of "Formulation 8".

3.2.2. Dynamic light scattering measurements

Dynamic Light Scattering (DLS), or Photon Correlation Spectroscopy, is a widely used technique to measure nanoparticle size and distribution in colloidal dispersions. DLS analyzes the Brownian motion of particles by measuring fluctuations in the intensity of scattered light, which correlate with particle diffusion rates—smaller particles diffuse faster, causing quicker intensity changes. Using the diffusion coefficient, DLS calculates the hydrodynamic diameter (dH) of particles. In this project DLS was used to determine liposomes' mean size (z-average) and polydispersity (PDI), the last indicates sample size uniformity. PDI values below 0.1 represent monodisperse (uniform) samples. The samples were diluted 50-fold with Milli-Q water, and three measurements were performed at 25 °C with an equilibration time of 60 seconds in a Zetasizer (Malvern Panalytical Ltd, UK). Each measurement consisted of 15 runs, each lasting 10 seconds, using a backscatter angle of 173°. The results were analyzed and processed using the ZS Xplorer v3.2.2.5 software (Malvern Panalytical Ltd).

3.2.3. Zeta potential measurements

Zeta potential is the electrostatic potential at the boundary, or "slipping plane," between a nanoparticle's surface-bound ions and those loosely associated with the surrounding solution. It reflects the effective surface charge of the nanoparticle in an ionic environment. By applying an electric field, the electrophoretic mobility of nanoparticles can be measured to calculate their zeta potential. This value is essential for understanding particle stability and interactions in colloidal systems. To measure zeta potential, an electric field is applied across the sample, inducing the nanoparticles to move according to their electrophoretic mobility. The Henry equation is used to calculate the zeta potential:

$$Ue = \frac{2\varepsilon\zeta f(\kappa a)}{3\eta}$$

where U_e is the electrophoretic mobility, ε is the dielectric constant, η is the absolute zero-shear viscosity of the medium, *f(κa)* is the Henry function, and *κa* is a measure of the ratio of the particle radius to the Debye length. Nanoparticles with a zeta potential between −10 and +10 mV are considered approximately neutral, while nanoparticles with zeta potentials greater than +30 mV or less than −30 mV are considered strongly cationic and anionic, respectively (67).

In this project, zeta potential measurements were carried out with a Zetasizer, and liposomes were diluted 100 times with Milli-Q water. The results were analyzed and processed using the ZS Xplorer v3.2.2.5 software.

3.2.4. Stewart assay for lipid quantification

The lipid content of each liposomal formulation was quantified according to the Stewart assay, which is based on the ability of phospholipids to form a colored complex with ammonium ferrothiocyanate in an organic solution. Indeed, the experimental setup needs two different phases. The aqueous phase consists of 2 mL of 0.1 M ammonium ferrothiocyanate solution (prepared by dissolving 27.03 g/L of $FeCl_3$ and 30.40 g/L of NH_4SCN in Milli-Q water), while the organic phase consists of 2 mL of chloroform (68). The color intensity of the complex is proportional to the lipid content in the solution.

The assay was performed by diluting a small aliquot of formulation in 2 ml of $CHCl_3$ and adding 2 mL of reagent ammonium ferrothiocyanate. After mixing the solution for 20 seconds with a vortex, centrifugation for 10 minutes at 1000 rpm was done, and the lower organic phase was analyzed with UV-Vis spectrophotometric measurement at 485 nm. The lipid concentration of each sample was extrapolated using a calibration curve prepared starting from a standard solution of 0.2 mg/mL lipid in chloroform, as reported in Table 3. The first stock was prepared with 0.2 mg/mL of corresponding lipid (HSPC or SPC), then 200 µL of this stock was added to 4.8 mL of chloroform to make the final stock for the calibration curve.

Stock solution	Chloroform	Ferrothiocyanate	Final concentration
0 mL	2 mL	2 mL	0 mg/mL
0.1 mL	1.9 mL	2 mL	0.01 mg/mL
0.2 mL	1.8 mL	2 mL	0.02 mg/mL
0.3 mL	1.7 mL	2 mL	0.03 mg/mL
0.4 mL	1.6 mL	2 mL	0.04 mg/mL
0.5 mL	1.5 mL	2 mL	0.05 mg/mL
0.6 mL	1.4 mL	2 mL	0.06 mg/mL
0.8 mL	1.2 mL	2 mL	0.08 mg/mL

Table 3: Stewart assay calibration curve.

3.2.5. RP-HPLC UV quantification method

The quantification of incorporated Vismodegib was performed using a reverse-phase high-performance liquid chromatography (RP-HPLC) method adapted from Calienni et al., 2019 (69). The flow rate was set to 1 mL/min, with the column temperature maintained at 35 °C, and the injection volume used was 10 µL. Elution was conducted using a gradient between two mobile phases: A (water + 0.05 % trifluoroacetic acid [TFA]) and B (acetonitrile [ACN] + 0.05 % TFA), as specified in Table 4. An Agilent 1260 Infinity HPLC system (Agilent Technologies, CA, USA), with a DAD detector, and coupled to a Jupiter® C18 column (3 µm, 300 Å, 150 × 4.6 mm, Phenomenex, CA, USA) was used for the RP-HPLC analysis.

Time (min)	A (%)	B (%)
0	85	15
12	50	50
13	5	95
14	5	95
15	85	15
20	85	15

Table 4: RP-HPLC mobile phase gradient.

Detection was carried out at a wavelength of 225 nm and a calibration curve for the standard drug was generated by 1/2 serial dilution in the mobile phase (85 % of A and 15% of B).

3.2.6. Incorporated drug quantification

The mass of the encapsulated Vismodegib into the liposomes was determined by RP-HPLC after complete disruption of 1 volume of formulation with 3 volumes of ACN. Initially, the disruption was done with different solvents including DMSO, MeOH, and ACN, and prepared twice to confirm which was the best. The results were nearly the same, so for this project, all the disruption steps were performed with ACN, to ensure a more similar medium as the mobile phase. The mixture was vortexed for 1 minute and centrifuged for 10 min at maximum rpm. The supernatant, diluted in the mobile phase, if necessary, was then analyzed by RP-HPLC.

3.2.6.1. Encapsulation efficiency (EE%)

The encapsulation efficiency was calculated as the percentage of the initial drug amount that was successfully encapsulated within the liposomes. It was determined using the formula:

$$EE\%: \frac{Encapsulated\ drug\ mass}{Total\ initial\ drug\ mass} \times 100$$

3.2.6.2. Drug-to-lipid ratio

The drug-to-lipid ratio was calculated by dividing the mass of the encapsulated drug by the total lipid mass in the formulation.

$$Drug\ to\ lipid\ ratio = \frac{Encapsulated\ drug\ mass}{Total\ lipid\ mass}$$

3.2.7. Long-term stability studies

In vitro stability tests were conducted on two batches of “Formulation 8” to evaluate liposome homogeneity over time. This involved assessing the mean particle size, PDI, and drug encapsulation efficiency. The liposomal formulations, containing 0.05% w/v NaN_3, were stored at 4 °C for two months. Drug quantification and DLS measurements were performed at specific intervals post-synthesis: 0, 7, 14, 30, and 60 days.

3.2.8. Transmission Electron Microscopy (TEM)

Transmission electron microscopy (TEM) was employed to examine the morphological and dimensional properties of the liposome formulation. This microscope operates by emitting a high-energy electron beam toward the sample and electrons penetrate it. The resolution limit depends on the instrument, but is approximately 0.5 nm, enabling magnifications of up to 100,000 times.

For visualizing liposomes, a negative staining with 1% uranyl acetate was carried out. The lipid concentration was around 0.2 mg/mL. The assay was done by the Microscopy Service of the Department of Biology of the University of Padova. The instrument used was a Tecnai G2 (FEI, OR, USA) microscope equipped with an OSIS Veleta 4K pixel camera.

3.2.9. Obtention of Atezolizumab's Fab'

As the aim of the project was to obtain immunoliposomes by conjugating the Fab' fragment of Atezolizumab antibody on the liposome surface, the Fab' was obtained by enzymatic digestion, reduction, and several purification steps.

The enzymatic digestion of the full antibody can be carried out using Pepsin. Pepsin cleaves the immunoglobulin at the hinge region, leading to the generation of the $F(ab')_2$ fragment from the intact antibody. Subsequently, further reduction of the disulfide bonds within the hinge region engenders two Fab' fragments, which can bind to the target PD-L1. This approach provides a functional Fab' fragment to use in further applications.

3.2.9.1 Enzymatic digestion of Atezolizumab using Pepsin and $F(ab')_2$ purification

Initially, the Pepsin enzyme was solubilized in acetate buffer (0.1 M, pH 3.8), vortex, and centrifuge for 2 minutes at 7000 rpm. Subsequently, the supernatant absorbance at 280 and 350 nm were measured by means of spectrophotometry ($\varepsilon = 1.35\ mL \times cm^{-1} \times mg^{-1}$) to calculate the concentration of enzyme (section 3.2.12.1). The absorbance at 280 nm was corrected by subtracting the absorbance at 350 nm, that is related with protein aggregates. The full antibody (MW = 145 kDa) was incubated with the Pepsin in acetate buffer (0.1 M, pH 3.8) for 30 minutes at 37 °C and 300 rpm, using an enzyme/substrate ratio of 1:50 w/w, providing the $F(ab')_2$ fragment separation from the Fc moiety of antibody (Figure 1).

Following the digestion, the reaction mixture was dialyzed overnight in a cold room under continuous stirring using a Slide-A-Lyzer G2 dialysis cassette 3,500 MWCO (Thermo Fisher Scientific, MA, USA) against phosphate buffer (10 mM, pH 6) to adjust the pH and stop Pepsin reaction. The following day, the pH of the dialyzed sample was checked with pH indicator paper to confirm pH change. The sample was filtered using Corning ® Costar ® Spin-X ® centrifuge tube (0.22 µm, cellulose acetate membrane) to remove aggregates. Then, $F(ab')_2$ was purified by cation exchange chromatography (CEX) using a TSKgel® SP-5PW column (10 µm, 7.5 mm × 7.5 cm, Tosoh Corporation, Japan) and a Prominence modular HPLC (Shimadzu Corporation, Japan) with a UV-Vis detector. The elution was carried out using a gradient between two mobile phases: A (phosphate buffer 10 mM, pH 6) and B (phosphate buffer 0.1 mM + NaCl 0.1 M, pH 6), as described in Table 5. The flow rate was 1 mL/min and the measurements were done at 226 and 280 nm.

Time (min)	A (%)	B (%)
0	100	0
10	95	5
65	0	100
80	0	100
85	95	5

Table 5: CEX-HPLC mobile phase gradient.

The purified $F(ab')_2$ was concentrated using Amicon® MWCO 30 kDa at 3500 rpm and 4 °C, samples were washed 3 times with PBS 1× EDTA 10 mM (pH 7.4) for exchanging the buffer, and the protein concentration was determined by BCA assay (section 3.2.12.2).

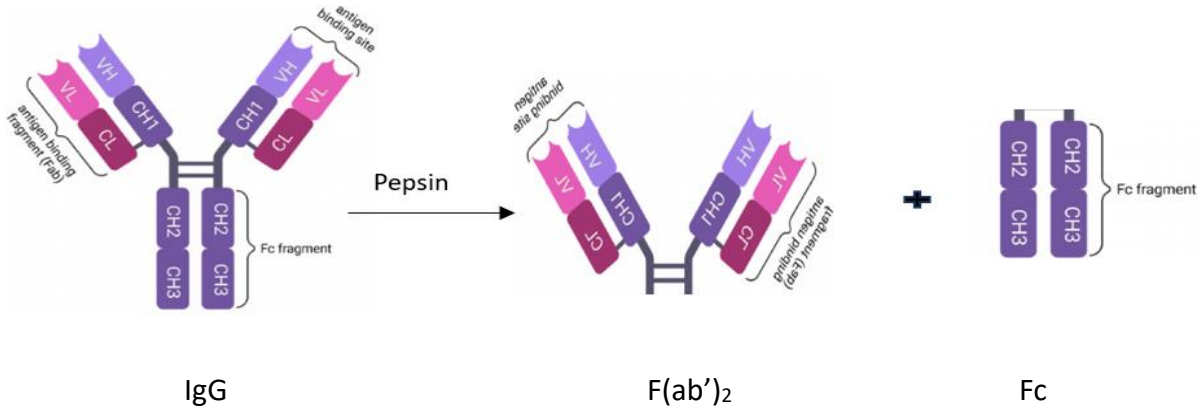

Figure 1: IgG digestion to $F(ab')_2$ and Fc fragments.

3.2.9.2. Reduction of Atezolizumab's F(ab')$_2$ to Fab'

The purified F(ab')$_2$ (~100 kDa) was incubated with 10 mM cysteamine (MW 113.61 Da) in PBS 1× EDTA 10 mM (pH 7.4) at 25 °C and F(ab')$_2$ concentration of 1 mg/mL, for 30 minutes to reduce the interchain disulfide bonds in the hinge region, separating the two Fab' fragments (Figure 2). The reaction mixture was filtered using Corning ® Costar ® Spin-X ® centrifuge tube (0.22 µm, cellulose acetate membrane) to remove aggregates. Subsequently, the Fab' was purified by size exclusion chromatography (SEC) with a Superdex 200 Increase 10/300 GL (Cytiva, Marlborough, MA) column by fast protein liquid chromatography (FPLC), in isocratic conditions with PBS 1× EDTA 10 mM (pH 7.4), at a flow rate of 0.5 mL/min, the detection was done at 280 nm. The FPLC used was an AKTA® Purifier FPLC system (GE Healthcare, Sweden). The purified Fab' was concentrated using Amicon® MWCO 30 kDa at 3500 rpm and 4 °C and the protein concentration was quantified by spectrophotometry.

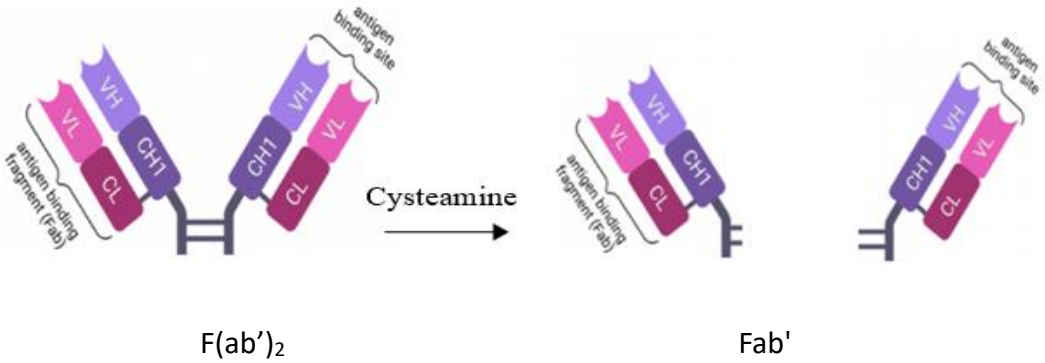

F(ab')$_2$ Fab'

Figure 2: F(ab')$_2$ reduction to Fab'.

3.2.10. PEGylation of Fab'

The next step after purifying the Fab' (~50 kDa) was to immediately do the reaction with the mal-PEG$_{5kDa}$-DSPE (MW = 5568 Da) to prevent as much as possible thiol groups reoxidation which could prevent PEGylation. The conjugation of the Fab' fragment of the antibody to mal-PEG$_{5kDa}$-DSPE was achieved through a thiol-maleimide reaction. The purified Fab' exposes free thiol (-SH) groups to conjugate to the mal-PEG$_{5kDa}$-DSPE through a stable thioether linkage (Figure 3). The reaction was carried out overnight in a molar ratio of 10:1 between mal-PEG$_{5kDa}$-DSPE and Fab' , with a final Fab' concentration of 1 mg/mL, at 25 °C and 300 rpm. To determine if the reaction was achieved, SDS-PAGE followed by iodine, coomassie blue, and

silver staining (section 3.2.13.3), as well as micro-BSA assay (section 3.2.12.2.) were carried out.

Additionally, the free maleimide groups that have not reacted with the Fab' were blocked with a thioglycolic acid solution in PBS at a 2:1 molar ratio to Fab'-PEG-DSPE. The reaction was carried out at 25 °C for 15 minutes and 300 rpm.

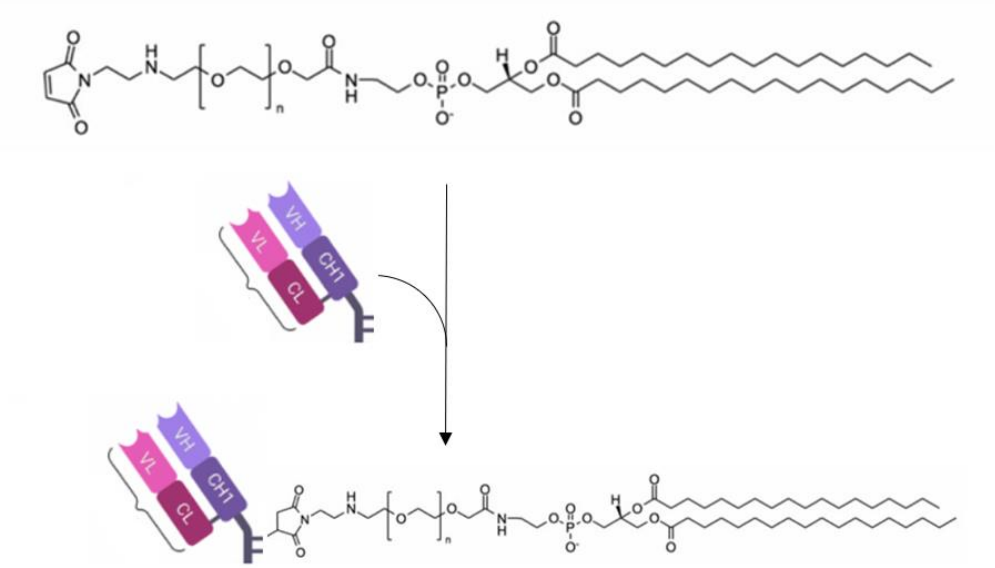

Figure 3: Fab' PEGylation with mal-PEG-DSPE.

3.2.11. Trastuzumab's Fab' purification

To optimize the conjugation of Fab' with maleimide groups on the liposome surface, the Fab' fragment of the Trastuzumab antibody was used as a model protein. Both antibodies are monoclonal IgG with similar structural characteristics, but different targets, leading to Trastuzumab to be suitable for optimizing the immunoliposome formulation.

The obtention of Trastuzumab's Fab' is similar to that of Atezolizumab but it has different incubation parameters and purification steps. Firstly, a buffer exchange was done with acetate buffer (0.1 M, pH=3.8) using Amicon® MWCO 30 kDa at 3500 rpm and 4 °C. The protein concentration was determined by UV-Visible spectrophotometry (Trastuzumab ε = 1.43 mL × cm^{-1} × mg^{-1}). Pepsin reaction was carried out in the same ratio, buffer, and temperature conditions as for Atezolizumab (section 3.2.9.1). In this case, the final concentration of the antibody has to be 15 mg/mL and the incubation time was 3 hours without agitation. The reaction mixture was filtered using Corning® Costar® Spin-X® centrifuge tube (0.22 µm,

cellulose acetate membrane) to remove aggregates. Then, the $F(ab')_2$ was purified by means of SEC-FPLC using a Superose 12 10/300 GL column (Cytiva, Marlborough, MA), under isocratic conditions with PBS (pH 7.4), a flow rate of 0.5 mL/min, and the detection was done at 280 nm. The collected sample was concentrated, and the buffer was exchanged to PBS 1× EDTA 10 mM (pH 7.4) using Amicon® MWCO 30 kDa at 3500 rpm and 4 °C, and the protein concentration was quantified by BCA assay. The reduction of $F(ab')_2$ to Fab' was also done with 10 mM cysteamine, 25 °C, without agitation, and 30 minutes, but the final protein concentration was 10 mg/mL. The reaction mixture was filtered using Corning® Costar® Spin-X® centrifuge tube (0.22 µm, cellulose acetate membrane), and the Fab' was purified by SEC-FPLC with a Superdex 200 Increase 10/300 GL column in the same conditions as those used for Atezolizumab (section 3.2.9.2). The purified Fab' was concentrated using Amicon® MWCO 30 kDa at 3500 rpm and 4 °C and the protein concentration was quantified by spectrophotometry. PEGylation of the Fab' was carried out immediately after purification under the same conditions indicated in section 3.2.10 for Atezolizumab.

3.2.12. Determination of protein concentration

Different analysis relies on precise quantitation of protein concentration, for this reason, in this section protein quantification assays employed in this project are described.

3.2.12.1. UV-Visible spectroscopy

In some cases, protein concentration was measured using a spectrophotometer (Evolution 201, Thermo Scientific, MA, USA) and measuring the absorbance at 280 nm. As mentioned before, the absorbance at 280 nm was corrected by subtracting the absorbance at 350 nm. The Atezolizumab's Fab' $\varepsilon = 1.70\ mL \times cm^{-1} \times mg^{-1}$ and for Trastuzumab's Fab' $\varepsilon = 1.35\ mL \times cm^{-1} \times mg^{-1}$.

3.2.12.2. BCA and micro-BCA assays

Protein concentration was assessed using the BCA assay, for detecting lower protein concentrations, the micro-BCA assay, a more sensitive variant, was used. BCA assay is a colorimetric method based on the reduction of Cu^{2+} ions from copper (II) sulfate (initially a green solution) by protein peptide bonds in a basic environment at 37 °C (Figure 4). In this reaction, Cu^{2+} is reduced to Cu^{+}, which subsequently reacts with BCA, forming a purple-colored complex with a strong absorbance at 562 nm (70). The absorbance and the intensity of the color change from green to purple are directly proportional to the protein concentration in the

solution.

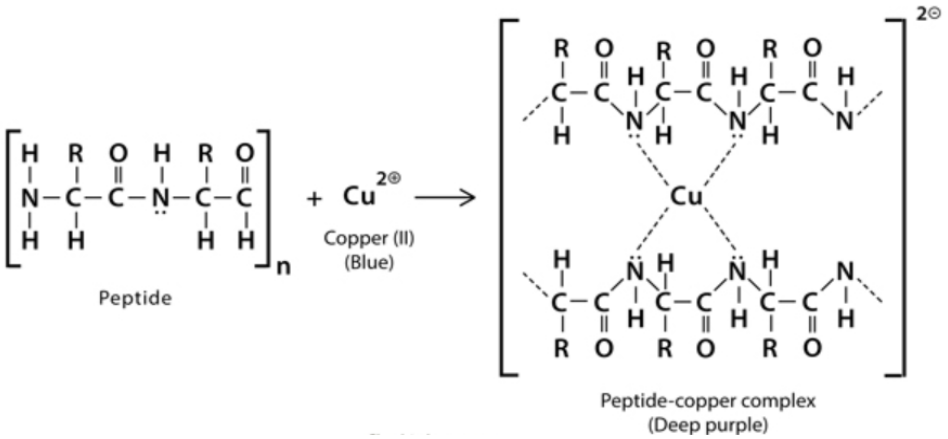

Figure 4: The reduction of Cu^{2+} ions by protein peptide bonds (71).

Protein samples were prepared in triplicate as outlined in Table 6 and 7 for BCA and micro-BCA, respectively, and incubated with the working reagent (WR) for 30 and 120 minutes, at 37 °C and 300 rpm. Absorbance was then measured at λ = 562 nm or 570 nm using a UV–Visible spectrophotometer for BCA and a microplate spectrophotometer (INNO-M, LTek Co. ltd, South Korea) for micro-BCA, respectively. For the BCA, the WR consists of a freshly prepared 50:1 v/v solution of bicinchoninic acid and $CuSO_4$, combined just before incubation with the protein samples. For the micro-BCA, 25 parts of a solution consisting of sodium carbonate, sodium tartrate, and sodium bicarbonate in 0.2M NaOH, pH 11.25, was mixed with 25 parts of a solution of 4% w/v bicinchoninic acid solution, pH 8.5. Then 1 part of 4% w/v $CuSO_4 \cdot 5H_2O$, and the mixture was vortexed until it was uniform in color.

For both antibodies $F(ab')_2$ quantification, a calibration curve was prepared using Trastuzumab within a concentration range of 0.1 to 0.6 mg/mL. If necessary, protein samples were diluted with PBS 1× EDTA 10Mm, pH 7.4.

Volume	Blank	Standard	Sample
450 µL	WR	WR	WR
20 µL	PBS 1× EDTA 10Mm, pH 7.4	0.1-0.6 mg/mL Trastuzumab	Protein Solution

Table 6: Preparation of samples for BCA assay.

Volume	Blank	Standard	Sample
75 µL	WR	WR	WR
75 µL	PBS 1× EDTA 10Mm, pH 7.4	1-20 µg/mL Trastuzumab	Protein Solution

Table 7: Preparation of samples for micro-BCA assay.

3.2.13. Sodium dodecyl sulfate-polyacrylamide gel electrophoresis (SDS-PAGE)

Polyacrylamide gel electrophoresis (PAGE) under denaturing conditions with sodium dodecyl sulfate (SDS) was employed for monitoring the different steps of Fab' obtention and purification, the PEGylation process, and the incorporation of Fab' on the liposome surface.

Generally, SDS binds to proteins, imparting a uniform negative charge. It enables their separation primarily based on molecular weight as they migrate through a polyacrylamide gel matrix under an electric field. The gel's pore size, which decreases with increasing acrylamide concentration, along with the protein's charge, size, and shape, collectively influences the migration rate (72).

SDS-PAGE was conducted by following standard laboratory protocol (73), using 4–15% Mini-PROTEAN® TGX™ Precast Protein Gels (Bio-Rad, CA, USA) and the molecular weight marker Precision Plus Protein Dual Color Standards (Bio-Rad, CA, USA). The running buffer consisted of 1× dilution from a 10× solution of 0.25 M Tris-HCl, 1.92 M Glycine, 1% w/v SDS, and pH 8.3. Samples were prepared by mixing 1 volume of sample with 1 volume of a non-reducing loading buffer 2× (Laemmli Sample Buffer, Bio-Rad, CA, USA) and were boiled at 100 °C for 3 minutes. Depending on the type of sample and staining, different protein masses were used. For iodine and coomassie, a mass of around 5 µg of protein was employed for non-PEGylated proteins and around 10 µg for PEGylated ones. For silver staining, the amount of non-PEGylated proteins was reduced by half. At the same time, also the amount of marker was reduced by half and diluted fourfold to prevent overstaining. On the other hand, the amount of samples from liposomal formulations was optimized to avoid interferences in the gel. The mass of lipids was maintained below 100 µg. Electrophoresis was conducted at 250 V and 60 mA. After running, the gel was stained with different techniques, as detailed below, to detect

proteins and PEG.

3.2.13.1 Iodine staining

Reversible iodine staining was performed, which allowed the visualization of both free and conjugated PEG-DSPE. The staining consists of the formation of a dark brown complex when PEG interacts with a $BaCl_2$ solution containing KI in acidic conditions.

To prepare the gel for PEG staining, residual bromophenol blue was removed by soaking the gel in a solution of 20 mL of water and 169 µL perchloric acid for 15 minutes. Once the bromophenol blue was completely cleared, a total of 5 mL of 5% w/v $BaCl_2$ and 1 M HCl solution, and 2 mL of 1.27% w/v I_2 and 2% w/v KI solution were added. The staining was stopped by removing the liquid and rinsing the gel in water. The iodine staining can be removed by adding a spatula tip amount of sodium L-ascorbate to the water.

3.2.13.2. Coomassie brilliant blue staining

Coomassie brilliant blue R-250 staining is a widely used method for detecting proteins on polyacrylamide gels. It is a triphenylmethane dye derivative in which the structure includes sulfonic acid groups that interact with proteins, particularly at basic and aromatic amino acid residues. Its sensitivity is around 0.1–0.5 µg protein.

After the SDS-PAGE or iodine destaining, the gel was immersed in a solution containing 0.1% coomassie brilliant blue R-250, 50% methanol, and 10% glacial acetic acid for two hours. Then, it was soaked with water for 30 minutes and placed in a destaining solution of 40% methanol and 7% glacial acetic acid until the background disappeared. Finally, the gel was thoroughly washed and stored in water.

3.2.13.3. Silver staining

Silver staining is the most sensitive and pivotal qualitative technique to define the presence and purity degree of proteins by SDS-PAGE. This method is approximately 100 times more sensitive than coomassie brilliant blue R-250 and the detection limit is 1–5 ng of protein per band.

The ProteoSilver Plus Silver Stain kit from Sigma-Aldrich was employed after doing some modifications after SDS-PAGE or coomassie staining. If the gel was not stained before, it was hydrated in water for 10 minutes and then immersed in the same destaining solution used in coomassie staining for at least one hour for fixing. If the coomasie staining was carried out before, the silver staining started from the next step. After fixation, the gel was washed with a

30% ethanol solution for 10 minutes, followed by a step of hydrating with water for 10 min. Then, the gel was soaked with the sensitizer solution for 10 minutes and washed twice with water for 10 minutes each time. It was incubated with the silver solution for 10 minutes and washed with water for only 1 minute. Finally, the gel was immersed in the developer solution for 3-7 minutes, and the reaction was stopped with a stop solution when protein bands appeared. The gel was washed and stored in water.

3.2.14. Immunoliposomes preparation

To obtain Vismodegib-loaded immunoliposomes targeting PD-L1 (VISMO-SIL), a post-insertion method was used to incorporate the Fab'-PEG_{5kDa}-DSPE to the Vismodegib-loaded stealth liposomes. The post-insertion method used was based on a previous group's protocol (not published yet) that consists of incubating the stealth liposomes with micelles that contain Fab'-PEG_{5kDa}-DSPE and m-PEG_{5kDa}-DSPE in PBS for 1 hour at 60 °C and 300 rpm. These last represent the 2% mol of the SPC concentration in the obtained VISMO-SL, being 1 part of Fab'-PEG_{5kDa}-DSPE and 3 parts of m-PEG_{5kDa}-DSPE. Similarly, vismodegib-loaded stealth liposomes were subjected to post-insertion without Fab'-PEG5kDa-DSPE to produce stealth liposomes (VISMO-SL) with the same PEGylation ratio as VISMO-SIL. Therefore, the micelles were composed of 2% mol respect of the SPC concentration of m-PEG_{5kDa}-DSPE.
After the post-insertion, the amount of drug retained in the liposomes was determined by RP-HPLC (section 3.2.5). Since the method used to incorporate Fab' significantly reduced the drug content, as demonstrated in the results section, alternative approaches were explored and are described below.

3.2.14.1. Alternative approaches for Fab' conjugation and post-insertion

3.2.14.1.1. First approach: changes in temperature and time

The post-insertion method was modified by decreasing the incubation temperature to 25°C and 40°C, which consequently extended the incubation periods. The different conditions tested are summarized in Table 8. This approach was conducted to assess the impact of temperature on the process. For this assay, only VISMO-SL were obtained, so the Vismodgib-loaded liposomes were incubated with micelles composed only of m-PEG_{5kDa}-DSPE in the same proportion as in section 3.2.14. The amount of drug retained was also assessed by RP-HPLC.

Temperature (°C)	Time (hours)	Agitation (rpm)
25	1	300
25	24	300
25	48	300
40	1	300
40	24	300
40	48	300

Table 8: Post-insertion conditions tested for the first new approach.

3.2.14.1.2. Second approach: VISMO-SL + Fab'-PEG$_{5kDa}$-DSPE

Another approach assessed was to incubate the Vismodegib-loaded liposomes only with the Fab'-PEG$_{5kDa}$-DSPE maintaining the same proportions and conditions as in the original protocol (section 3.2.14) (Figure 5). The amount of drug retained was assessed by RP-HPLC.

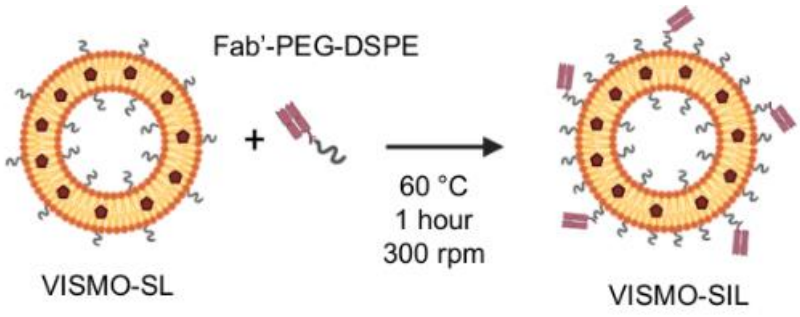

Figure 5: Schematic representation of the VISMO-SIL obtention through the incubation of VISMO-SL with Fab'-PEG$_{5kDa}$-DSPE.

3.2.14.1.3. Third approach: VISMO-L + Fab'-PEG$_{5kDa}$-DSPE and VISMO-L + Fab'-PEG$_{5kDa}$-DSPE + m-PEG$_{5kDa}$-DSPE

Alternatively, non-stealth liposomes (VISMO-L) were obtained in the same manner as "Formulation 8" (Tables 1 and 2) without the inclusion of the m-PEG$_{5kDa}$-DSPE. These

VISMO-L were subjected to the post-insertion approaches detailed in sections 3.2.14 and 3.2.14.1.2 (Figure 6). The amount of drug retained was assessed by RP-HPLC.

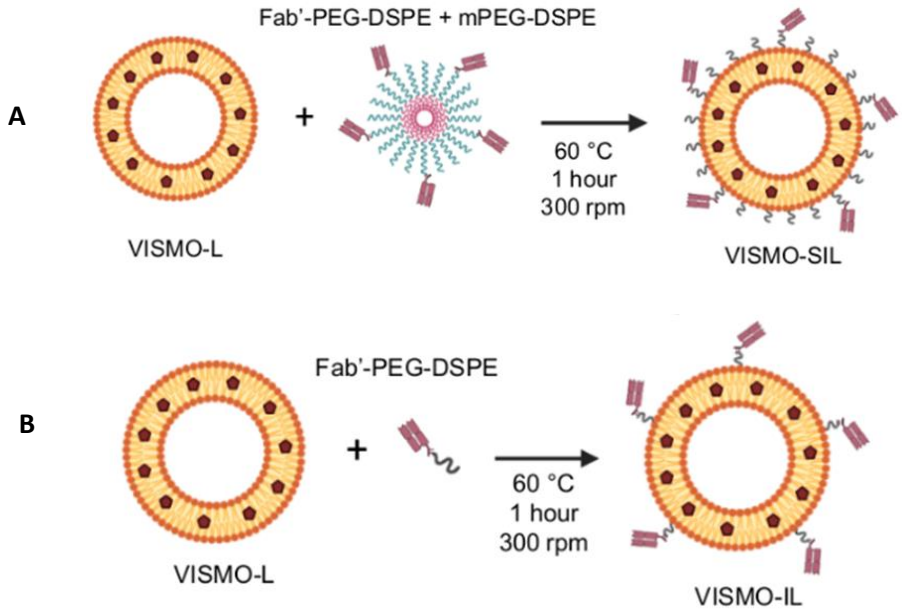

Figure 6: Schematic representation of the VISMO-SIL obtention through the incubation of VISMO-L with Fab'-PEG$_{5kDa}$-DSPE + m-PEG$_{5kDa}$-DSPE (A) and the incubation of VISMO-L with Fab'-PEG$_{5kDa}$-DSPE (B).

3.2.14.1.4. Fourth approach: Fab'-PEG$_{5kDa}$-DSPE addition during the hydration of the lipid film

This approach was also assessed based on the results of the other approaches. The lipid film was prepared as detailed for "Formulation 8" (Tables 1 and 2) but with the addition of Fab'-PEG$_{5kDa}$-DSPE during the hydration step (Figure 7) in the double proportion considered for the post-insertion (section 3.2.14).It was doubled to account for the portions that also interact with the inner membrane. The Fab'-PEG$_{5kDa}$-DSPE was previously dissolved in PBS. The amount of drug retained was assessed by RP-HPLC.

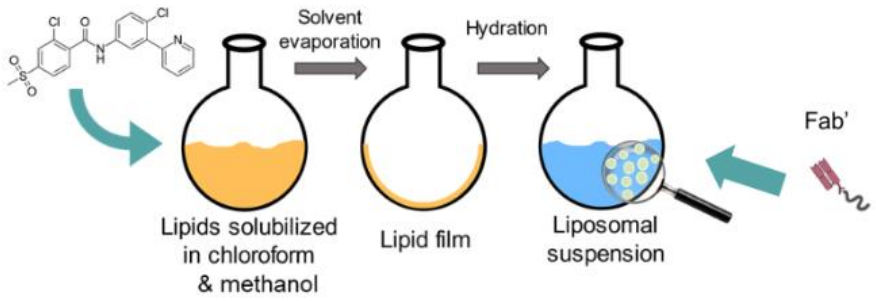

Figure 7: Schematic representation of the obtention of VISMO-SIL by adding the Fab'-PEG$_{5kDa}$-DSPE during the film hydration step.

3.2.14.1.5. Fifth approach: VISMO-SL + Fab'

The last approach evaluated aimed to avoid post-insertion, as it was shown to decrease the amount of encapsulated drug. For this reason, VISMO-SL was directly incubated with the non-PEGylated Fab' (Figure 8). However, "Formulation 8" (Tables 1 and 2) did not contain maleimide reactive groups, so it was reformulated such that mal-PEG$_{5kDa}$-DSPE was incorporated into the liposomes during their formation, as shown in Table 9. The amount of mal-PEG$_{5kDa}$-DSPE added was double that used in the post-insertion methods, considering that some maleimide groups remain on the inner membrane surface. The incubation conditions were similar to those for Fab' PEGylation. The reaction was carried out overnight in a molar ratio of 10:1 between the theoretical amount of maleimide groups on the liposome surface and Fab' at 25 °C and 300 rpm. The amount of drug retained was assessed by RP-HPLC.

Components	Molecular weight	Mass	Molar ratio
SPC	775.03 Da	0.03 gr	100
m-PEG$_{5kDa}$-DSPE	6116 Da	0.01461 gr	6
mal-PEG$_{5kDa}$-DSPE	5568 Da	0.00216 gr	1
Vismodegib	421.3 Da	0.003 gr	18

Table 9: Composition of 2 ml of VISMO-SL for direct conjugation of Fab'.

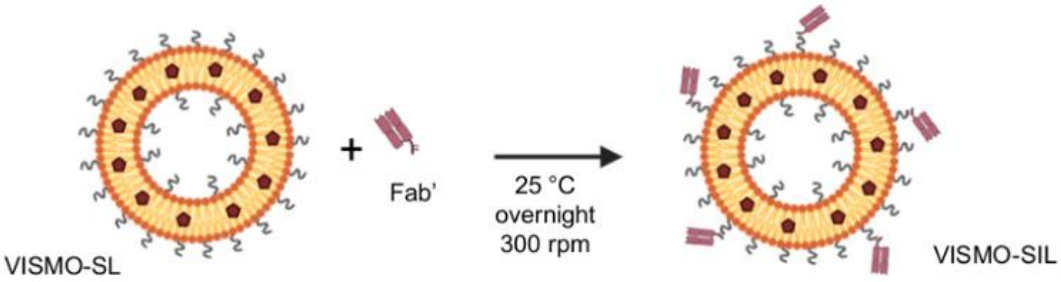

Figure 8: Schematic representation of the conjugation reaction between VISMO-SL containing maleimide groups on the surface of the liposomes and Fab' for the obtention of VISMO-SIL.

Finally, this approach was the selected method for the VISMO-SIL synthesis and for carrying out the cytotoxicity studies with.

3.2.15. Cytotoxicity assessment

The cytotoxicity of the obtained formulation was assessed on two different human cell lines: the HaCaT cell line, consisting of transformed keratinocytes from histologically normal skin, and the SK-Mel-28 cell line, consisting of melanoma cells. Both cell lines present the Hh signaling pathway active (74,75). and were selected to determine if there are differential effects between tumor and non-tumor cells. The cells were grown under adhesion conditions and were maintained at 37 °C with 5% CO_2 in DMEM (HaCaT) or EMEM (SK-Mel-28) supplemented with 10% heat-inactivated fetal bovine serum (FBS), 2 mM L-glutamine, 10^5 Units/L penicillin G sodium, and 100 mg/L streptomycin sulfate.

The experiments were carried out in collaboration with Prof. Sara De Martin, Department of Pharmaceutical Sciences, University of Padova.

3.2.15.1. Viability evaluation by Crystal Violet assay

A screening on the range of vismodegib concentration that decrease cell viability after 48 hours of treatment was carried out using the crystal violet (CV) assay in triplicate. It is based on the ability of viable cells to adhere to a surface and retain the dye that binds to DNA and proteins. Cells undergoing cell death lose their adherence, which reduces the amount of CV staining in the culture. Therefore, changes in the absorbance of the solution of dye after the assay can be related to cell viability.

A total of 1 x 10^4 cells/well were seeded in flat-bottom 96-well microplates. The following day, the culture medium was replaced with 100 µl of samples to be tested, previously diluted in fresh culture medium. Due to the hydrophobic nature of the drug, a solution of the drug was prepared in DMSO, ensuring that the maximum concentration of vismodegib tested did not exceed 1% v/v DMSO in the well. Untreated controls were incubated with the same volume of fresh medium, and a control treated with 1% DMSO were included. Wells without cells were also included. The concentration range tested was 4-360 µM.

After the incubation, the medium was removed, the wells were washed with 200 µl of PBS, 50 µl/well of CV solution was added, and the plate was agitated in the dark at room temperature for 20 minutes to allow dye uptake. Following this, the wells were thoroughly washed with water and dried at 37 °C. Once dried, 200 µl/well of methanol was added to dissolve the crystals. Finally, the absorbance was measured at 570 nm using a VICTOR Nivo multimode microplate reader (Revvity, MA, USA).

The percentage of cell viability was determined according to the following equation, where absorbance T corresponds to the treated cells and absorbance C corresponds to the control cells (no treated):

$$\text{Cell viability (\%)} = \frac{Absorbance\ T}{Absorbance\ C} \times 100$$

The half-maximal inhibitory concentration (IC50) was determined by applying non-linear regression to a sigmoidal dose-response curve, where the concentration of vismodegib was plotted on a logarithmic scale against the percentage of viable cells, using GraphPad Prism 8.0.1 software (CA, USA).

2.15.2. Cytotoxicity studies with ATP-lite assay

The *in vitro* cytotoxic activity of the liposomes was tested using the ATP-lite assay (Perkin Elmer, MA, USA). The ATP-lite assay is a luminescence-based method used to evaluate cell viability. The luciferase enzyme catalyzes the oxidative carboxylation of luciferin, producing luminescence as shown as follows. A higher ATP concentration results in greater luminescence, indicating higher cell viability.

$$ATP + \text{D-luciferin} + O_2 \rightarrow \text{Oxyluciferin} + AMP + PPi + CO_2 + \text{Light}$$

For the experiment, 1 x 10^4 cells were seeded in black flat-bottom 96-well plates. The following day, the culture medium was replaced with 100 µl of the samples to be tested, previously diluted

in fresh culture medium. Vismodegib in DMSO (maximum DMSO concentration of 0.5% in the well), VISMO-SIL (section 3.2.14.1.5), the corresponding VISMO-SL (Table 9), and stealth liposomes without the drug (SL) were tested. For the Vismodegib-loaded formulations, the range of drug tested was 7-360 µM. The SL were diluted in the culture medium to achieve the same lipid concentrations as VISMO-SL. Untreated controls were included and incubated with the same volume of fresh medium. After 48 hours of incubation, the medium was removed, the wells were washed with 100 µl of PBS, 50 µl/well of lysis solution was added and the microplate was agitated for 5 minutes at 160 rpm. A total of 50 µl/well of ATP-lite solution, was added and the microplate was firstly agitated in the dark for 5 minutes and 160 rpm, and then incubated for another 10 minutes without agitation. The luminescence was measured in a microplate reader. The percentage of cell viability was determined according to the following equation, where luminescence T corresponds to the treated cells and luminescence C corresponds to the control cells (no treated):

$$\text{Cell viability (\%)} = \frac{Luminescence\ T}{Luminescence\ C} \times 100$$

Additionally, the IC50 was determined.

4. RESULTS

4.1. VISMO-SL characterization and optimization

As described in Section 3.2.1, various formulations were analyzed to optimize VISMO-SL. The dH, Z-average, and PDI were measured using DLS, with most formulations yielding values around 100 nm despite minor variations. Notably, all formulations exhibited a single, unimodal peak in the DLS measurements, indicating uniform size distribution. For most formulations, a pellet was observed at the bottom of the Eppendorf tube, likely to represent drug precipitation due to leakage. However, "Formulation 8", which was composed of SPC: $mPEG_{5kDa}$-DSPE: Vismodegib with a molar ratio of 16:1:0.4 demonstrated superior drug retention and incorporation without noticeable precipitation, making it the chosen formulation for further studies (Table 1,2). The DLS size distribution graphs for "Formulation 8" are shown in Figure 1.

Formulation	Z-Average (nm)	PDI
Formulation 1	119.3 ± 0.6	0.029 ± 0.0082
Formulation 2	115.1 ± 0.5	0.060 ± 0.0172
Formulation 3	105.1 ± 0.8	0.046 ± 0.0207
Formulation 4	71.9 ± 0.3	1.112 ± 0.0214
Formulation 5	102 ± 0.4	0.058 ± 0.0113
Formulation 6	97.5 ± 0.7	0.028 ± 0.0242
Formulation 7	104 ± 0.9	0.038 ± 0.0171
Formulation 8	101 ± 1.3	0.020 ± 0.0139
Formulation 9	99.9 ± 0.9	0.031 ± 0.0247

Table 1: DLS results of all evaluated VISMO-SL.

Formulation	Encapsulation efficiency	Incorporated drug (mg/mL)	Lipid (mg/mL)	Drug/lipid ratio (w/w)
Formulation 1	5.6 %	0.047	15.6	1:332
Formulation 2	21.7 %	0.156	22.7	1:145
Formulation 3	22.7 %	0.193	19.2	1:99
Formulation 4	42.1 %	0.178	22.6	1:127
Formulation 5	36.4 %	0.299	20.8	1:69
Formulation 6	73.6 %	0.351	15.6	1:44
Formulation 7	93 %	0.221	14.6	1:66
Formulation 8	105.8 %	0.362	20.15	1:55
Formulation 9	100.7 %	0.302	22.04	1:73

Table 2: Drug incorporation and lipid concentration of the prepared formulations.

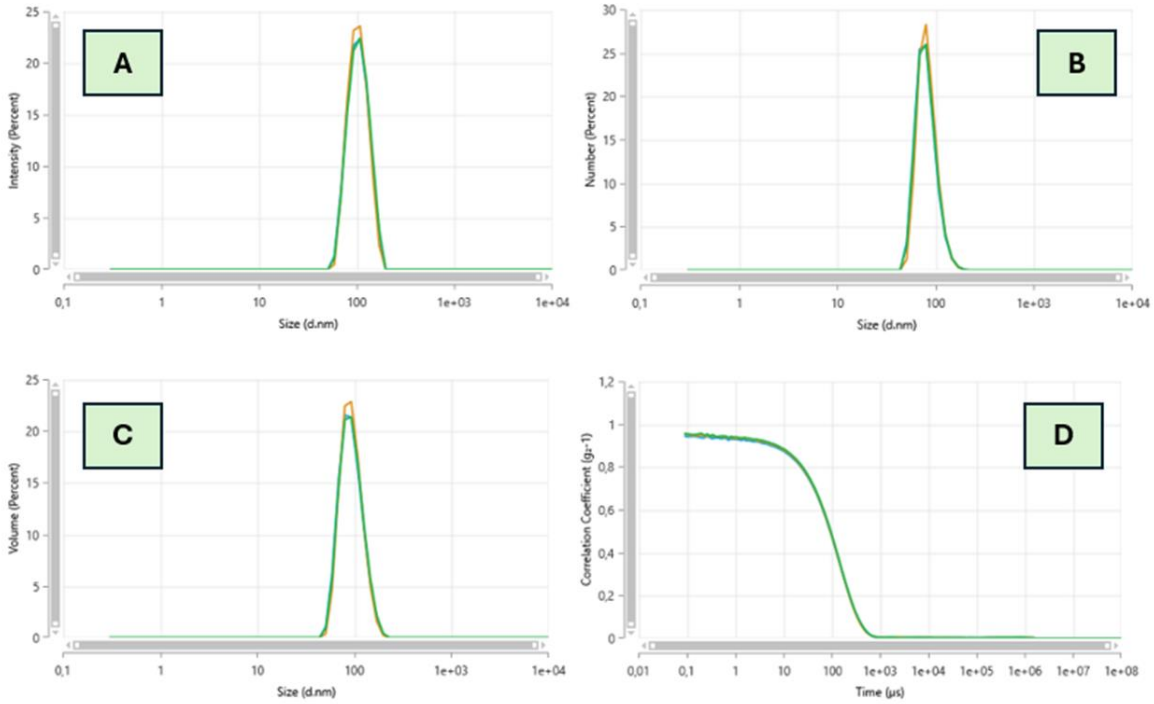

Figure 1: DLS results for a single batch of freshly prepared "Formulation 8". The data are presented as the percentage of size distribution by intensity (A), number (B), and volume (C) relative to size (nm), along with the correlogram showing the correlation coefficient versus time (µs) (D).

4.2. Stability studies of the Formulation 8 over time

To evaluate the stability of the formulation over time, "Formulation 8" was prepared in duplicate and monitored over a two-month storage period at 4 °C. No significant changes were observed in the size or PDI of the formulation. However, a moderate reduction in drug retention was observed, with the incorporated drug quantified by comparing it to the amount at time zero. Despite this, the overall encapsulation efficiency remained satisfactory (Table 3, Figure 2).

Days after preparation	Z-Average	PDI	Drug (µg/mL)	EE%
0	100.2 ± 1.6	0.03872 ± 0.01546	309 ± 6	105 ± 2
7	100.7 ± 2.3	0.03156 ± 0.00021	204 ± 12	72 ± 9
14	100.9 ± 0.2	0,02217 ± 0,00010	274 ± 10	79 ± 3
30	103.1 ± 2.5	0.02882 ± 0.00836	232 ± 34	67 ± 10
60	104.9 ± 0.7	0.03754 ± 0.02019	223 ± 50	64 ± 14

Table 3: Physicochemical characterization of two "Formulation 8" batches over time. Data are presented as mean ± standard deviation.

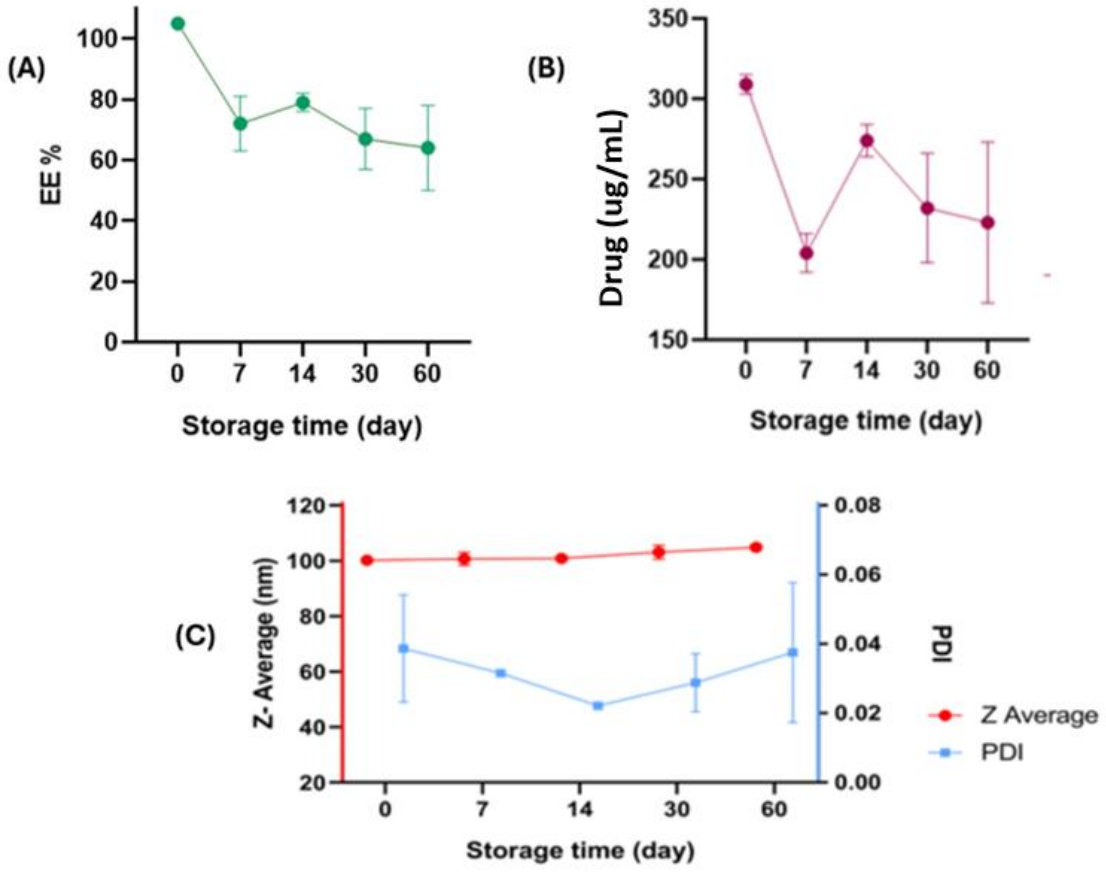

Figure 2: Physicochemical characterization of two "Formulation 8" batches over time. Data are presented as mean ± standard deviation. EE% (A), drug concentration (B), Z-Average, and PDI (C).

4.3 Characterization by TEM

The morphology and size of VISMO-SL were evaluated using TEM (Figure 3). The images showed spherical particles, as expected, and confirmed the size range determined by DLS.

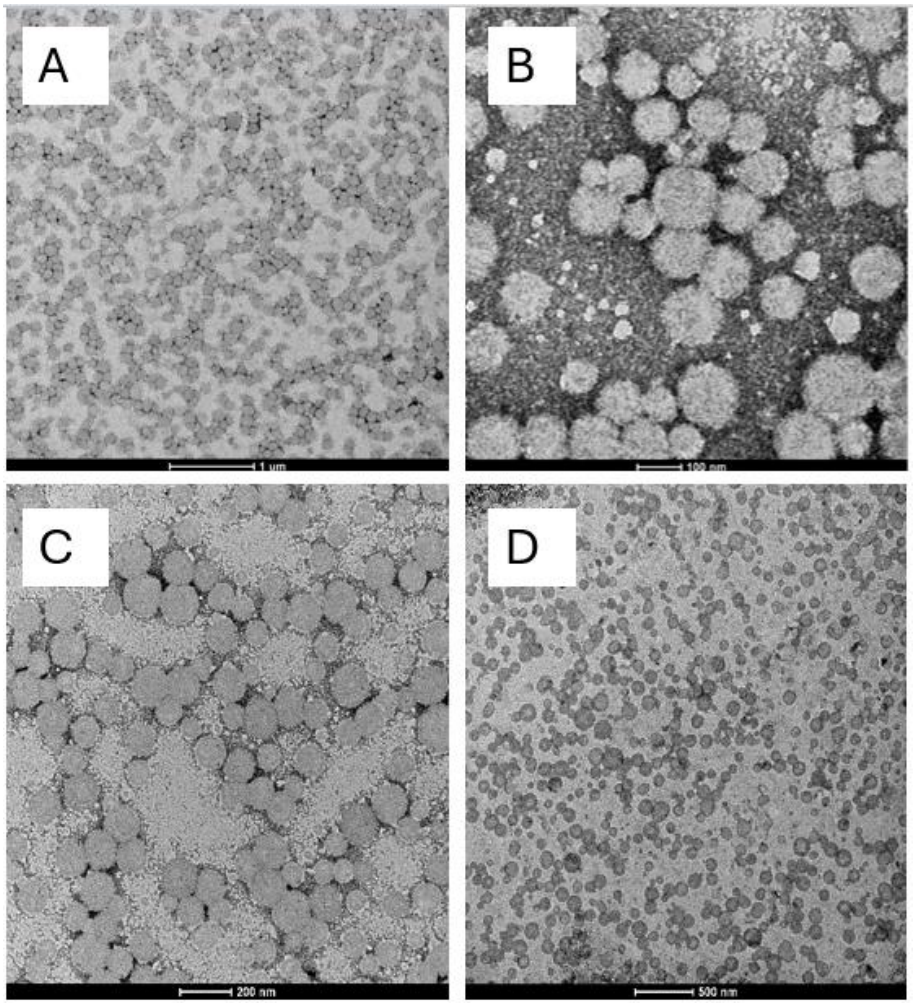

Figure 3: Representative TEM images of VISMO-SL at different magnifications. The scale bars correspond to 1µm (A), 100 nm (B), 200 nm (C), and 500 nm (D), respectively.

4.4 Atezolizumab's Fab' purification

4.4.1. Atezolizumab reduction to F(ab')$_2$

The antibody was incubated with Pepsin to obtain the F(ab')$_2$ fragment, and purification was performed using CEX-HPLC. As shown in Figure 4, the largest peak in the chromatogram corresponded to the F(ab')$_2$. This was confirmed by comparing the results with those from previous lab projects and further validated through SDS-PAGE gel, which showed a band with the corresponding molecular weight of around 100 kDa (Figure 6).

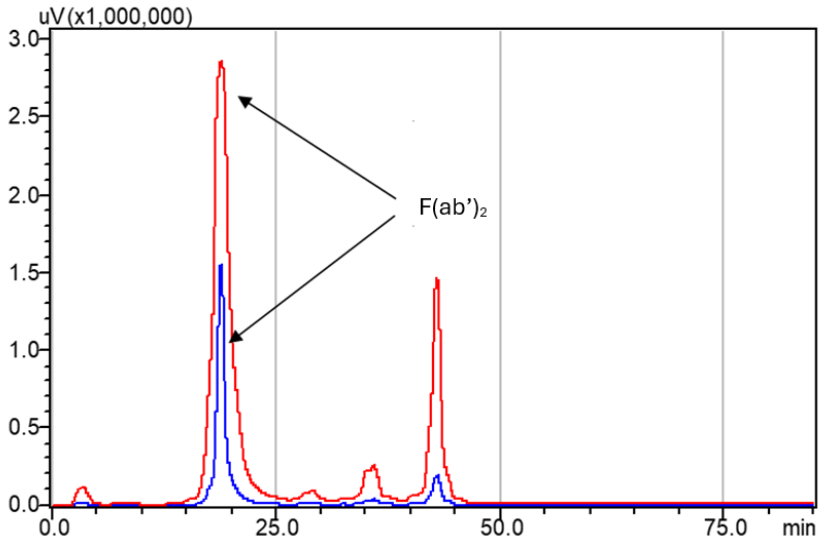

Figure 4: CEX-HPLC chromatogram of the Atezolizumab's F(ab')$_2$ fragment purification. The red line represents the signal at 226 nm, while the blue line represents the signal at 280 nm. Arrows indicate the F(ab')$_2$ peak at both wavelengths.

4.4.2. F(ab')$_2$ reduction to Fab'

The next step was the reduction of F(ab')$_2$ to Fab', by incubating the F(ab')$_2$ with cysteamine. The sample was purified by SEC-FPLC (Figure 5). As mentioned before, the corresponding Fab' peak was confirmed by comparing the results with those from previous lab projects and further validated through SDS-PAGE gel (Figure 6), which showed a band with the corresponding molecular weight of around 50 kDa. The presence of bands around 25 kDa can be attributed to the separation of the antibody's heavy and light chains. When the disulfide bonds connecting these chains are reduced the two chains are separated.

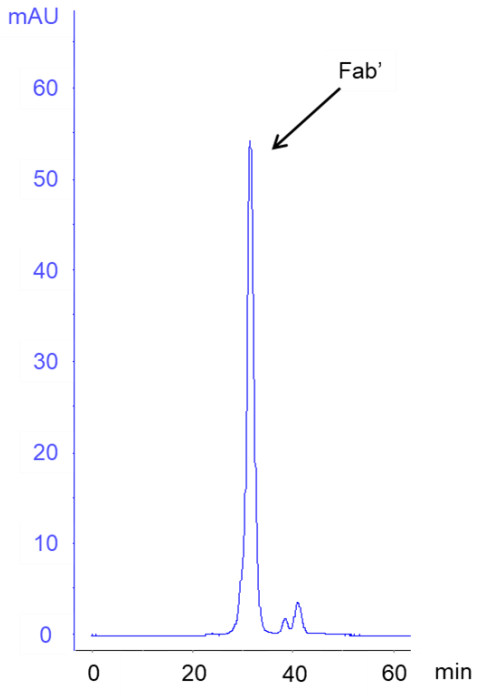

Figure 5: SEC-FPLC chromatogram of the Atezolizumab's Fab' fragment purification. The arrow indicates the Fab' peak.

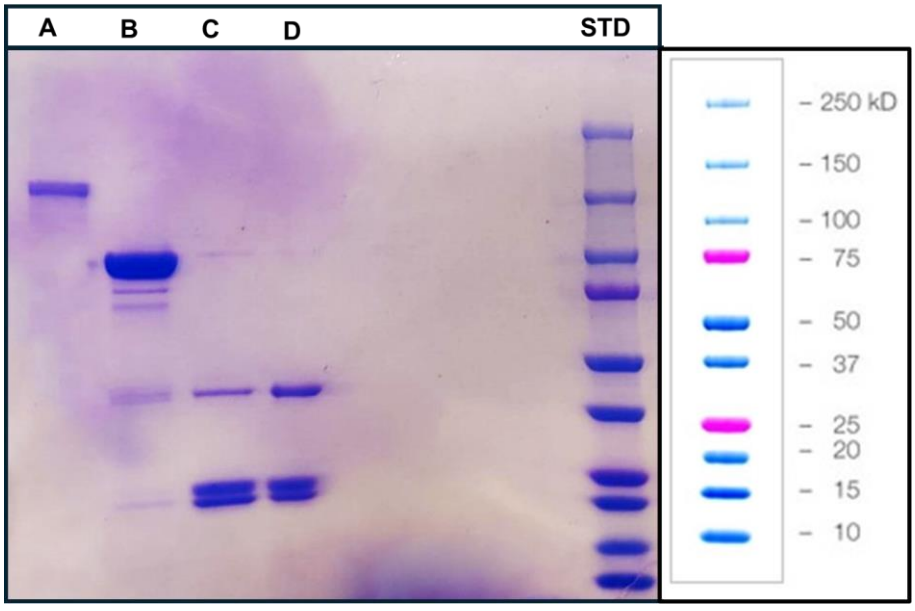

Figure 6: SDS-PAGE under non-reducing conditions, followed by coomassie blue staining. Samples were loaded in the following order: Atezolizumab (A), F(ab')$_2$ (B), Fab' (C and D), and molecular weight marker (STD).

4.4.3. Atezolizumab’s Fab' PEGylation

Depending on the protocol used for incorporating Fab' onto the liposome surface, two different PEGylation procedures were performed. In both cases, PEGylation was carried out immediately after purification and confirmed by SDS-PAGE followed by iodine, coomassie blue, and silver staining. Both protocols were conducted under identical conditions for temperature, agitation, and duration. The key difference was whether PEGylation occurred using micelles of mal-PEG_{5kDa}-DSPE or mal-PEG_{5kDa}-DSPE that were pre-incorporated into the liposomal bilayer during liposome preparation. Figure 7 presents an SDS-PAGE performed to confirm each step of Atezolizumab’s Fab' purification and PEGylation using mal-PEG_{5kDa}-DSPE micelles. Gels obtained for the direct conjugation of Fab' to liposome surface will be shown later. The gel image demonstrates the analysis of Fab' fragments and their PEGylation using Coomassie staining and iodine staining. The Coomassie stain reveals the presence of Fab' fragments, while the iodine stain specifically detects PEG-related components from the same reactions. The free PEG, though it has a molecular weight of approximately 5 kDa, typically appears as a band around 10 kDa on the gel, indicating the presence of unbound PEG in the sample. Additionally, the iodine stain confirms the formation of mono-, bi-, and tri-PEGylated Fab' fragments, which are visible as distinct bands corresponding to their progressively higher molecular weights due to the attachment of one, two, or three PEG molecules. This analysis confirms the presence of unmodified Fab', free PEG, and various PEGylated Fab' species.

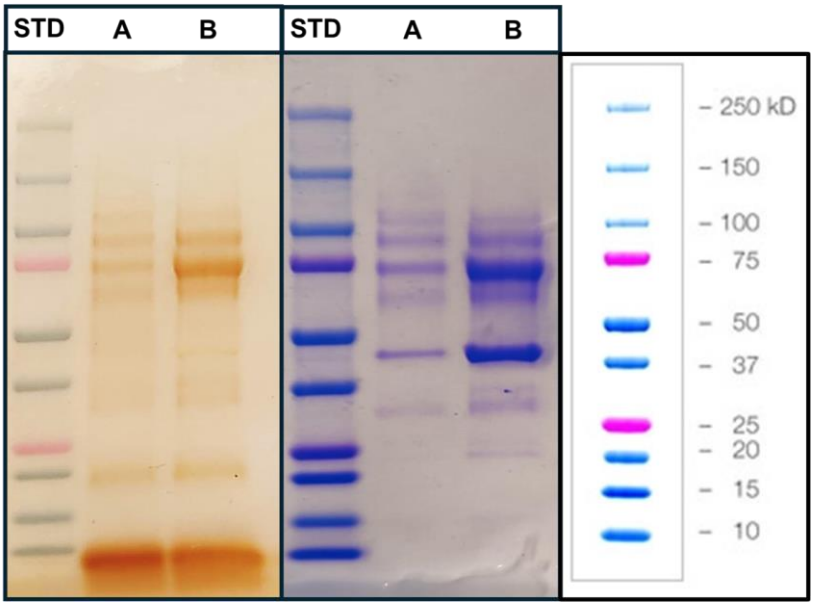

Figure 7: SDS-PAGE under non-reducing conditions, followed by iodine staining (left) and coomassie blue staining (right). Samples were loaded in the following order: molecular weight marker (STD) and Atezolizumab's Fab'-PEG_{5kDa}-DSPE from two PEGylation reactions (A) and (B).

4.5. Trastuzumab's Fab' purification

4.5.1. Trastuzumab reduction to $F(ab')_2$

The antibody was incubated with Pepsin to obtain the $F(ab')_2$ fragment, and purification was performed using SEC-FPLC (Figure 8). The corresponding $F(ab')_2$ peak was confirmed by comparing the results with those from previous lab projects and further validated through SDS-PAGE gel, which showed a band with the corresponding molecular weight of around 100 kDa (Figure 10).

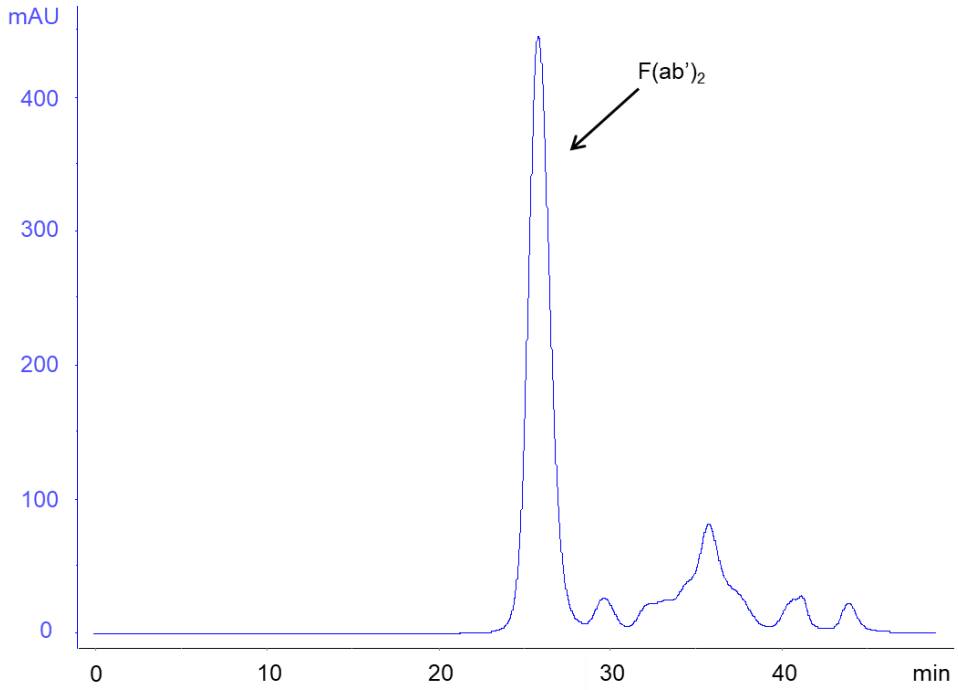

Figure 8: SEC-FPLC chromatogram of the Trastuzumab's F(ab')$_2$ fragment purification. The arrow indicates the F(ab')$_2$ peak.

4.5.2. F(ab')$_2$ reduction to Fab'

The F(ab')$_2$ was reduced to Fab' by the reaction with cysteamine. The obtained Fab' was purified by SEC-FPLC (Figure 9). The corresponding Fab' peak was confirmed by comparing the results with those from previous lab projects and further validated through SDS-PAGE gel (Figure 10), which showed a band with the corresponding molecular weight of around 50 kDa. Also here separation between the two chains of the Fab' happened and lower molecular weight bands were observed.

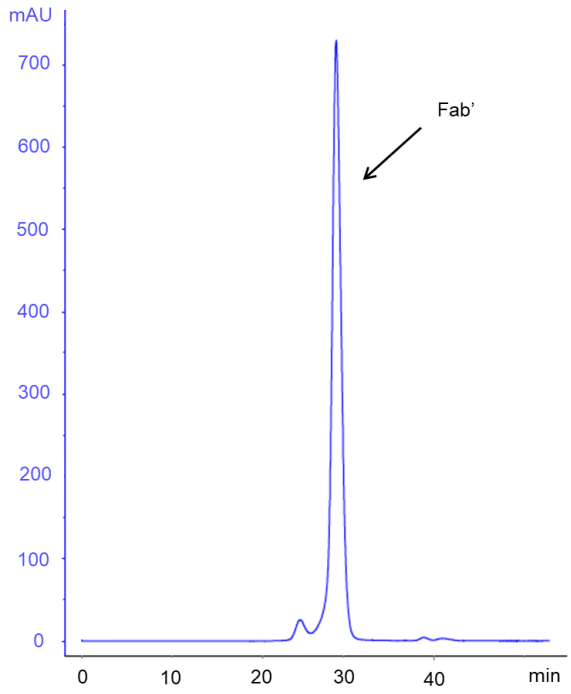

Figure 9: SEC-FPLC chromatogram of the Trastuzumab's Fab' fragment purification. The arrow indicates the Fab' peak.

4.5.3. Trastuzumab's Fab' PEGylation

The Fab' fragments were incorporated onto the liposome surface according to a specific protocol, followed by PEGylation. The PEGylation process was performed immediately after purification and verified through SDS-PAGE analysis, using iodine, coomassie blue, and silver staining. All steps were carried out under controlled conditions, with fixed parameters for temperature, agitation, and duration. Then to confirm the purification and PEGylation process the SDS-PAGE gel electrophoresis was also done. The results clearly showed the expected bands for different antibody components and their PEGylated forms. The Trastuzumab was visible at 150 kDa, while the $F(ab')_2$ fragment appeared at 100 kDa, and the Fab' was detected at 50 kDa. Additionally, the separation of the Fab' heavy and light chains was observed around 25 kDa. For the PEGylated samples, the biPEGylated forms were more prominent compared to the monoPEGylated forms, both for the whole Fab' and for its separated heavy and light chains. This indicates successful PEGylation with a stronger presence of biPEGylated species (Figure 10).

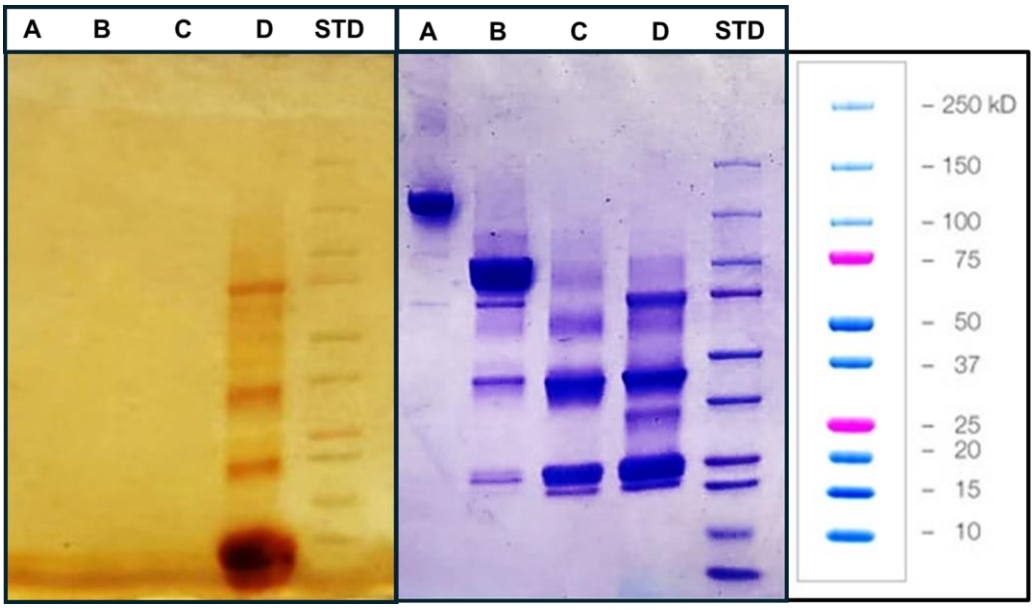

Figure 10: SDS-PAGE under non-reducing conditions, followed by iodine staining (left) and coomassie blue staining (right). Samples were loaded in the following order: Trastuzumab (A), F(ab')$_2$ (B), Fab' (C), Fab'-PEG$_{5kDa}$-DSPE (D), and molecular weight marker (STD).

4.6. First immunoliposomes obtention

Formulation 8 was subjected to the post-insertion method employed by our group to incorporate an antibody's Fab' to the liposome surface (section 3.2.14). Briefly, it consisted of the incubation of VISMO-SL with micelles composed of Fab'-PEG$_{5kDa}$-DSPE and m-PEG$_{5kDa}$-DSPE for 1 hour at 60 °C under agitation. As a control, the corresponding VISMO-SL formulation underwent the same post-insertion process but was incubated with micelles composed exclusively of m-PEG5kDa-DSPE. After the post-insertion, in both cases, liposomes were disrupted and the amount of drug was quantified by RP-HPLC (Table 4). The lipid concentration was assessed to also compare the drug-to-lipid ratio. The post-insertion decreased significantly the amount of drug in the liposomes. The reduction was around 78% with respect to the VISMO-SL before post-insertion.

Since the method used to incorporate the Fab' significantly reduced the drug content, alternative approaches were explored.

Formulation	Encapsulation efficiency	Drug (mg/mL)	Lipid (mg/mL)	Drug/lipid ratio (w/w)
VISMO-SL*	104.7 %	0.308	15	1 : 49
VISMO-SL**	22.2 %	0.061	21	1: 344
VISMO-SIL	19.4 %	0.057	13	1 : 228

Table 4: Drug and lipid concentration of VISMO-SL before (*) and after (**) post-insertion with micelles of m-PEG$_{5kDa}$-DSPE and VISMO-SIL after post-insertion with micelles of Fab'-PEG$_{5kDa}$-DSPE/m-PEG$_{5kDa}$-DSPE for 1 hour at 60 °C.

4.7. Alternative approaches for Fab' conjugation and post-insertion

As detailed in the methods section, different approaches were attempted to achieve a high amount of drug encapsulation after the incorporation of the Fab' on the liposome surface. The first one consisted of the incubation of VISMO-SL with m-PEG$_{5kDa}$-DSPE micelles varying the temperature and time of incubation. A total of three time points at 25 and 48 °C were tested. For all the conditions, the drug was not detectable.

The second approach consisted of only incubating the VISMO-SL with micelles of Fab'-PEG$_{5kDa}$-DSPE in the same conditions as the standard post-insertion protocol. However, one more time, the post-insertion even of a lower amount of conjugated lipids significantly decreased the encapsulated drug (Table 5).

Since the post-insertion process seemed to be causing the escape of Vismodegib from the liposomal membrane, the third strategy proposed consisted of obtaining non-PEGylated VISMO-L and trying the two different attempts of standard post-insertion: with the mixed micelles of Fab'-PEG$_{5kDa}$-DSPE + m-PEG$_{5kDa}$-DSPE and only with the Fab'-PEG$_{5kDa}$-DSPE. As reported in Table 5, these two post-insertion approaches slightly increased the concentration of the drug compared to the previous post-insertion attempts, but the amount of drug retained continued to be limited. Additionally, the post-insertion also in this case reduced significantly the amount of drug compared to the formulation before the post-insertion process (VISMO-SL, EE% = 64 % and drug concentration = 0.189 mg/mL).

Another strategy was to directly incorporate the Fab'-PEG$_{5kDa}$-DSPE during the hydration step of the lipid film to directly obtain liposomes with the Fab' and avoid post-insertion. The

disadvantage of this approach is that some Fab' are positioned in the inner surface of the bilayer and to conserve similar amounts of Fab' exposed in the external liposome surface, the proportion of Fab'-PEG_{5kDa}-DSPE had to be duplicated. The retention of Vismodegib in this case was better than all the previous approaches, reaching an encapsulation efficiency of around 30%. However, in a last attempt to improve the concentration of the drug in the formulation, a fifth approach was carried out and consisted of the direct conjugation of Fab' on the liposome surface. This was possible by obtaining VISMO-SL that presented maleimide groups on the liposome surface. This last attempt showed the best results without drug leaks. For the fifth approach, the incorporated drug was also determined for the VISMO-SL, because their composition included mal-PEG_{5kDa}-DSPE, not present in the previous VISMO-SL that were prepared with only m-PEG_{5kDa}-DSPE. In this case, VISMO-SL presented high encapsulation efficiency and a similar drug concentration as the VISMO-SL without maleimide groups (EE% = 119 %, drug concentration = 0.317 mg/mL).

Therefore, the cytotoxicity assays were carried out using the VISMO-SIL obtained by means of the fifth approach.

Approach	**Mix of reaction**	**Reaction conditions**	**Encapsulation efficiency**	**Drug (mg/mL)**	**Lipid (mg/mL)**	**Drug/lipid ratio (w/w)**
Second (post-insertion)	VISMO-SL + Fab'-PEG_{5kDa}-DSPE	60 °C, 1 hour, 300 rpm	0.4 %	0.0013	20.4	1 : 15692
Third (post-insertion)	VISMO-L + Fab'-PEG_{5kDa}-DSPE + m-PEG_{5kDa}-DSPE	60 °C, 1 hour, 300 rpm	7 %	0.0207	15	1 : 725
Third (post-insertion)	VISMO-L + Fab'-PEG_{5kDa}-DSPE	60 °C, 1 hour, 300 rpm	10 %	0.0321	15	1 : 467

Fourth (pre-insertion)	Fab'-PEG_{5kDa}-DSPE	Room temperature and vortex	29%	0.140	24	1 : 171
Fifth (direct conjugation)	VISMO-SL (with maleimide groups exposed) + Fab'	25 °C, overnight, 300 rpm	117%	0.310	16.5	1 : 53

Table 5: Drug and lipid concentration of the different VISMO-SIL obtained through different attempts for incorporating the Atezolizumab's Fab'. Some strategies implied post-insertion, another the incorporation of the PEGylated Fab' during the lipid film hydration, and another the direct conjugation of the Fab' with the maleimide groups on the liposome surface.

4.8. Evaluation of the Fab' conjugation with the mal-PEG_{5kDa}-DSPE on the liposome surface

The conjugation of the antibody's Fab' was evaluated using SDS-PAGE followed by iodine, coomassie blue, and silver staining. The optimization process was initially conducted with Trastuzumab and subsequently repeated successfully with Atezolizumab.

During the optimization of the conjugation between Fab' and the maleimide groups on the liposome surface, it was observed that, despite using protein quantities expected to be detectable by SDS-PAGE, the bands corresponding to Fab' and conjugated Fab' were not visible (Figure 11). Additionally, staining in all three methods (iodine, coomassie blue, and silver) was observed in the well where VISMO-SIL was loaded, suggesting that the sample did not migrate properly through the gel. For this reason, the lipid mass loaded onto the gel was optimized by testing different amounts of the same sample (Figure 12). It was observed that a high lipid content, typically associated with larger sample volumes that require concentration by evaporation before being loaded onto the gel, interfered with the normal migration of proteins.

Conversely, smaller lipid amounts did not cause interference, allowing the expected protein bands to be detected (Figure 12). Therefore, the direct conjugation of the Fab' on liposome surface was successfully achieved.

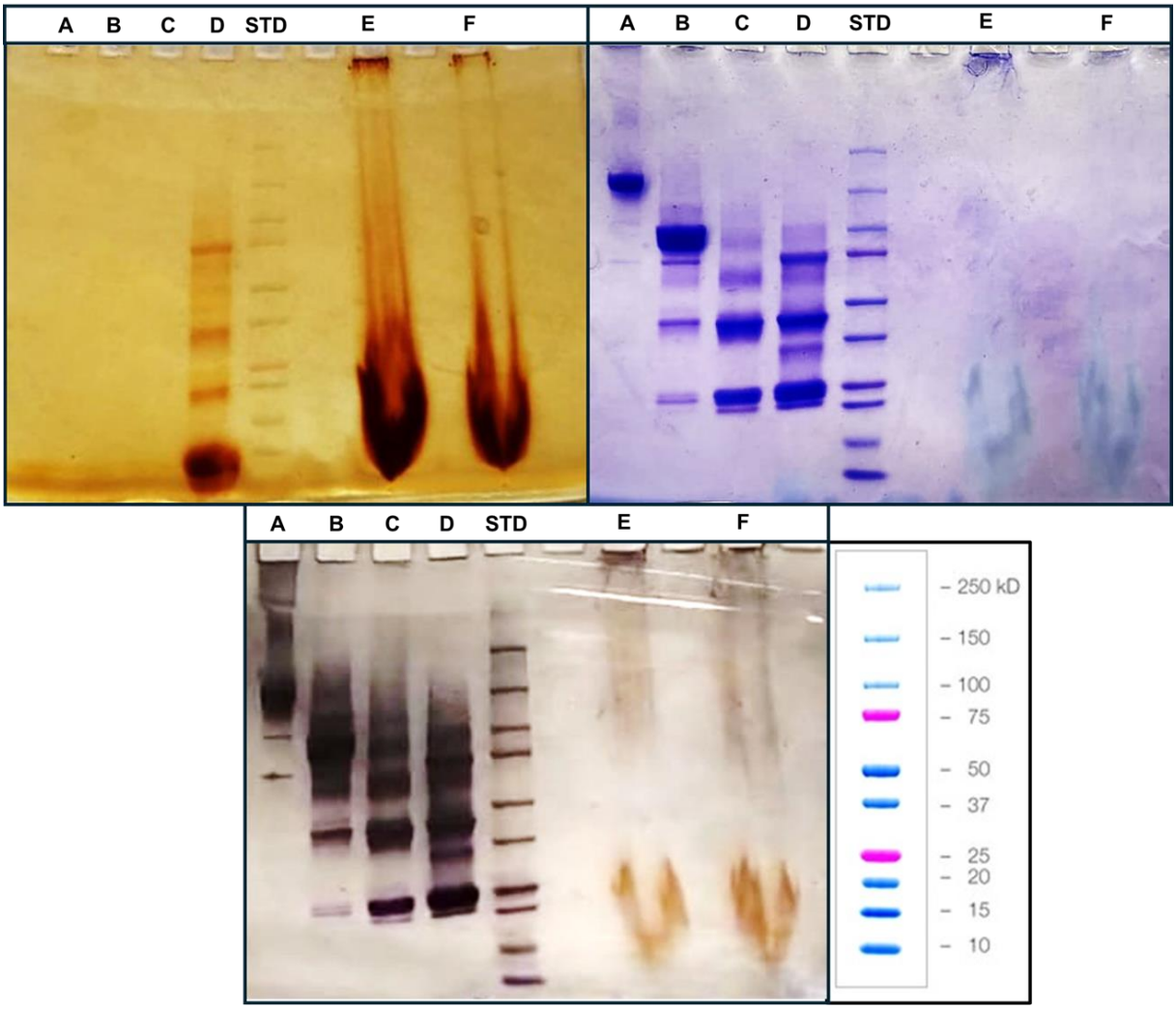

Figure 11: SDS-PAGE under non-reducing conditions, followed by iodine staining (upper left), coomassie blue (upper right), and silver staining (below). The three stains were carried out on the same gel. Samples were loaded in the following order: Trastuzumab (A), F(ab')$_2$ (B), Fab' (C), Fab'-PEG$_{5kDa}$-DSPE (D), molecular weight marker (STD), and VISMO-SIL (E and F).

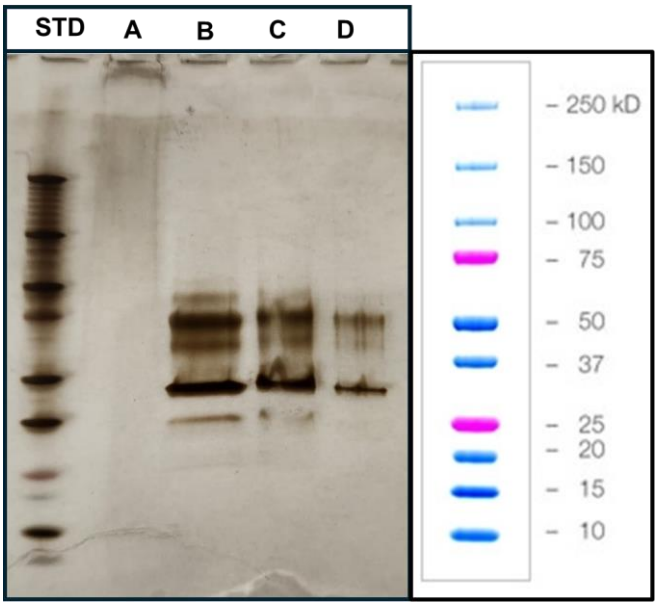

Figure 12: SDS-PAGE under non-reducing conditions, followed by silver staining of different lipid concentrations of VISMO-SIL obtained from the Trastuzumab's Fab' conjugation with the maleimide groups on VISMO-SL surface. Samples were loaded in the following order: molecular weight marker (STD), and different mass of lipid: 366 µg (A), 146 µg (B), 73 µg (C), and 37 µg (D).

Once the optimal protein-to-lipid ratio was determined, the same experiments were carried out but with the Atezolizumab's Fab' and the direct Fab' conjugation on the liposome surface was corroborated by SDS-PAGE (Figure 13). VISMO-SIL and, as a control, the corresponding VISMO-SL were loaded in the gel. In the same gel, the samples from all the steps of the Fab' obtention were run also to evaluate the purification process. The Atezolizumab full antibody (~150 kDa) as well as the $F(ab')_2$ (~100 kDa), and Fab' fragments (~50 kDa) were observed. The reduction of Fab' into its separated light and heavy chains was also observed (~25 kDa). On the other hand, there were observed bands corresponding to PEGylated Fab' in the VISMO-SIL sample, absent in the VISMO-SL as expected. Particularly, the most intense bands in the iodine staining were those corresponding to the mono and bi-PEGylated Fab'(~60 and 70 kDa). A light band can be also observed near 37 kDa, which can be related to the PEGylation of single Fab' chains. In the coomassie blue and silver staining could be observed an additional band around 50 kDa could be assigned to non-conjugated Fab'. Therefore, the direct Fab' conjugation to the VISMO-SL surface was successfully achieved.

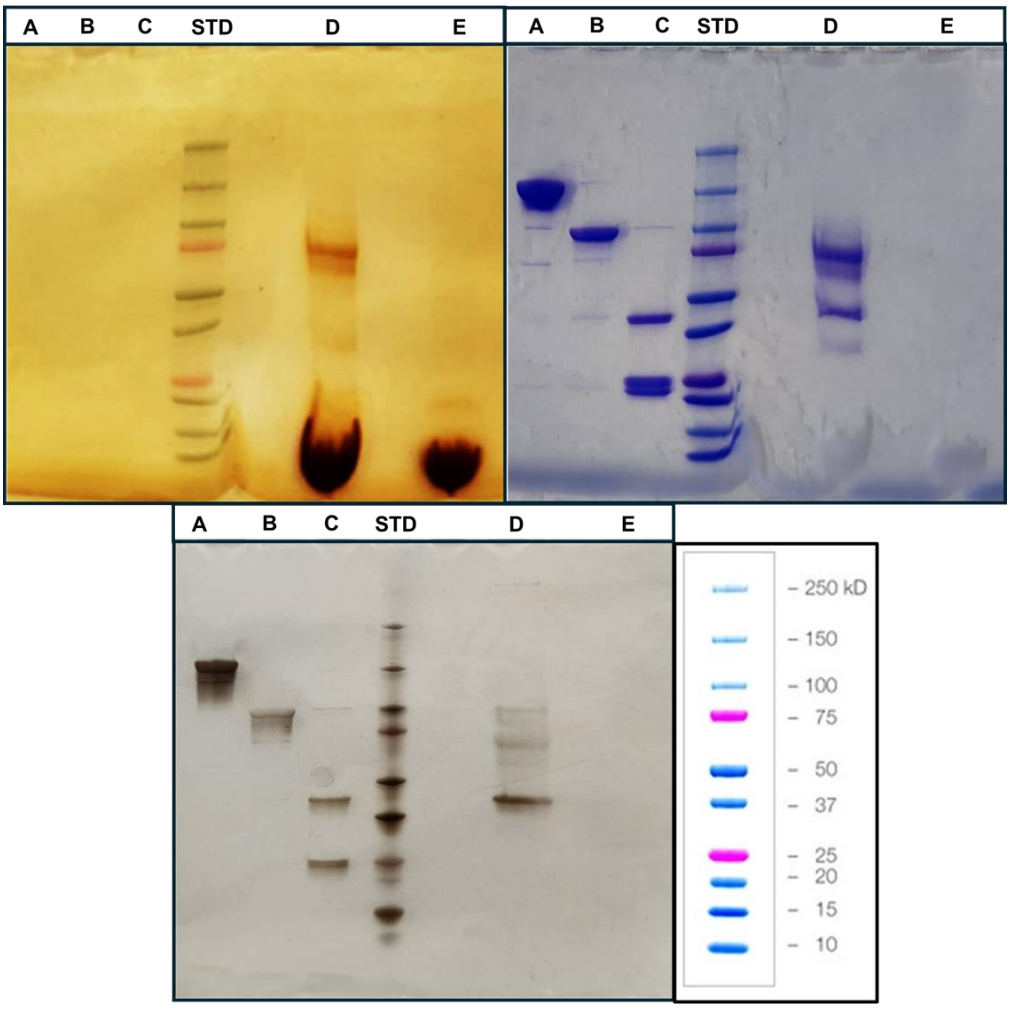

Figure 13: SDS-PAGE under non-reducing conditions, followed by iodine staining (upper left), coomassie blue (upper right), and silver staining (below). The iodine and coomassie blue staining were carried out on the same gel. Samples were loaded in the following order: Atezolizumab (A), F(ab')$_2$ (B), Fab' (C), molecular weight marker (STD), VISMO-SIL (D), and VISMO-SL (E).

4.9. VISMO-SIL physicochemical and morphological characterizations

Micro-BCA assay was used to quantify the concentration of Fab' conjugated to the liposomes and to calculate the Fab'-to-lipid ratio for the VISMO-SIL. The concentration of Fab' was 0.702 mg/mL and the Fab'/lipid ratio (w/w) was calculated as 1:23.

DLS measurements were also performed (Figure 14) and the zeta potential was determined. A summary of the main physicochemical features of both VISMO-SL and VISMO-SIL is shown in Table 6. The conjugation of the Fab' slightly increased the mean size of the liposomes and changed significantly the zeta potential making it more negative. Moreover, compared to

"Formulation 8," which had a zeta potential of -2.47 ± 0.41, the addition of maleimide and the Fab' resulted in a significantly more negative zeta potential.

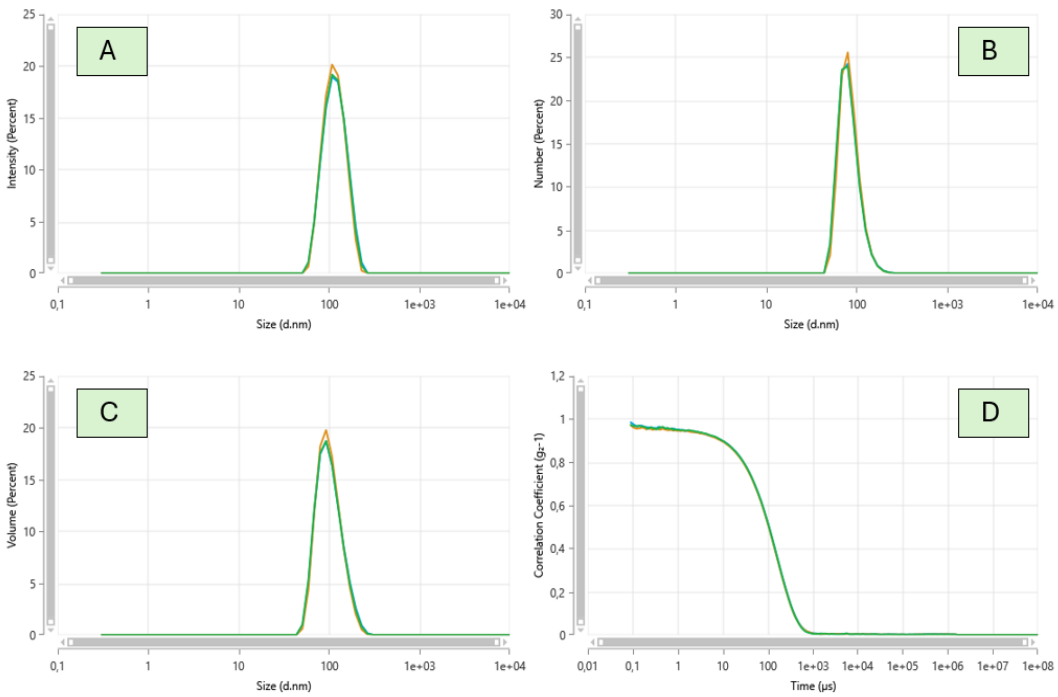

Figure 14: DLS results for single batch of Vismo-SIL. The data are presented as the percentage of size distribution by intensity (A), number (B), and volume (C) relative to size (nm), along with the correlogram showing the correlation coefficient versus time (µs) (D).

Formulation	Z-Average (nm)	PDI	Zeta potential (mV)
VISMO-SL	104.9 ± 0.48	0.02 ± 0.01	-21.81 ±2.2
VISMO-SIL	110.3 ± 1.05	0.06 ± 0.009	-23.58 ± 2.7

Table 6: The physicochemical properties of two Vismo-SL and Vismo-SIL.

On the other hand, TEM images were obtained to evaluate the morphology and size (Figure 15). The images showed spherical particles, as expected, and confirmed the size range determined by DLS.

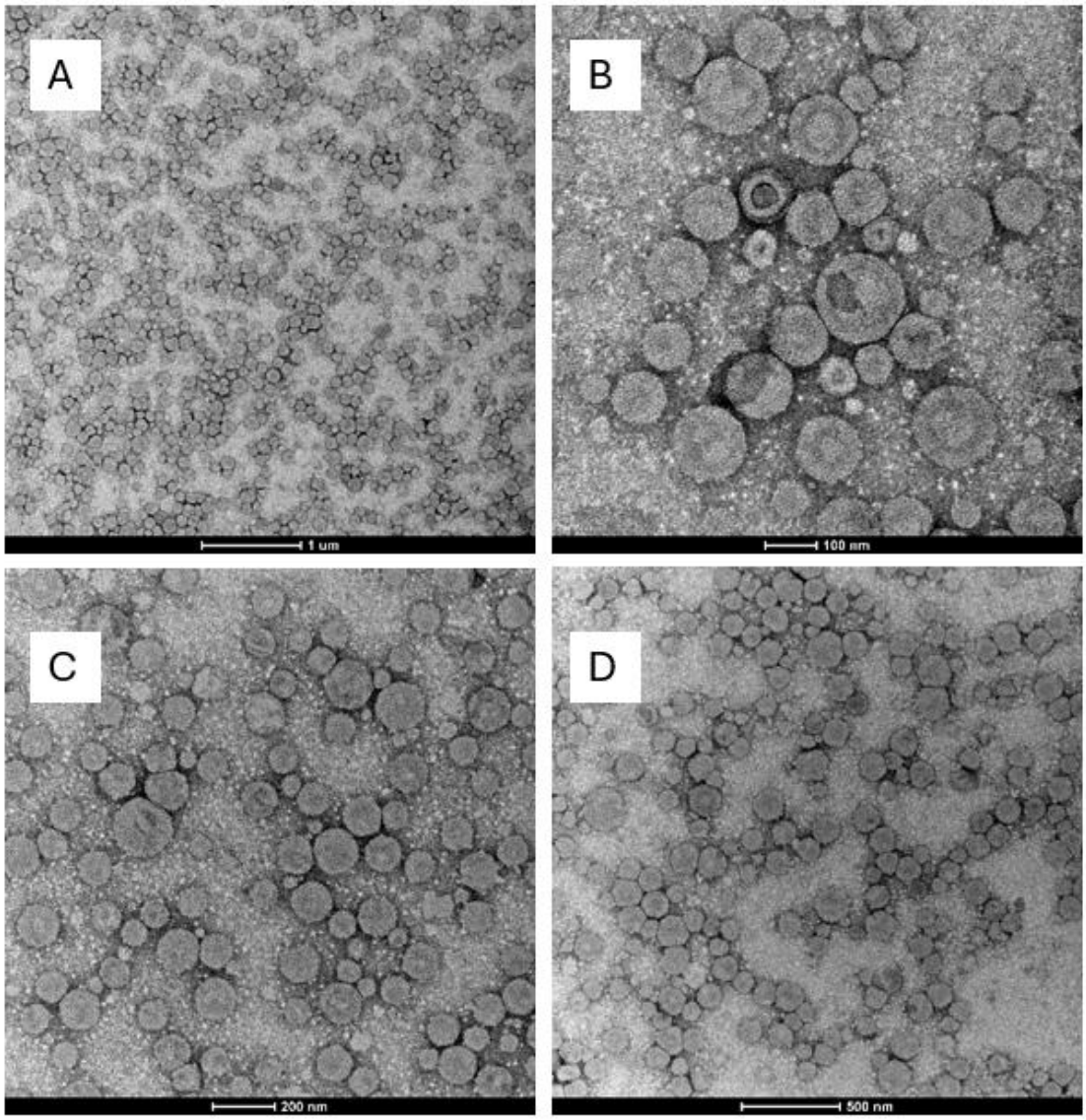

Figure 15: Representative TEM images of VISMO-SIL at different magnifications. The scale bars correspond to 1µm (A), 100 nm (B), 200 nm (C), and 500 nm (D), respectively.

4.10. Cytotoxicity assays

4.10.1 Cells morphology

The cells were detached and reseeded once every two days, and Figure 16 shows their normal morphology observed under the microscope. Keratinocytes are more regularly shaped, while melanoma cells are often elongated and irregular.

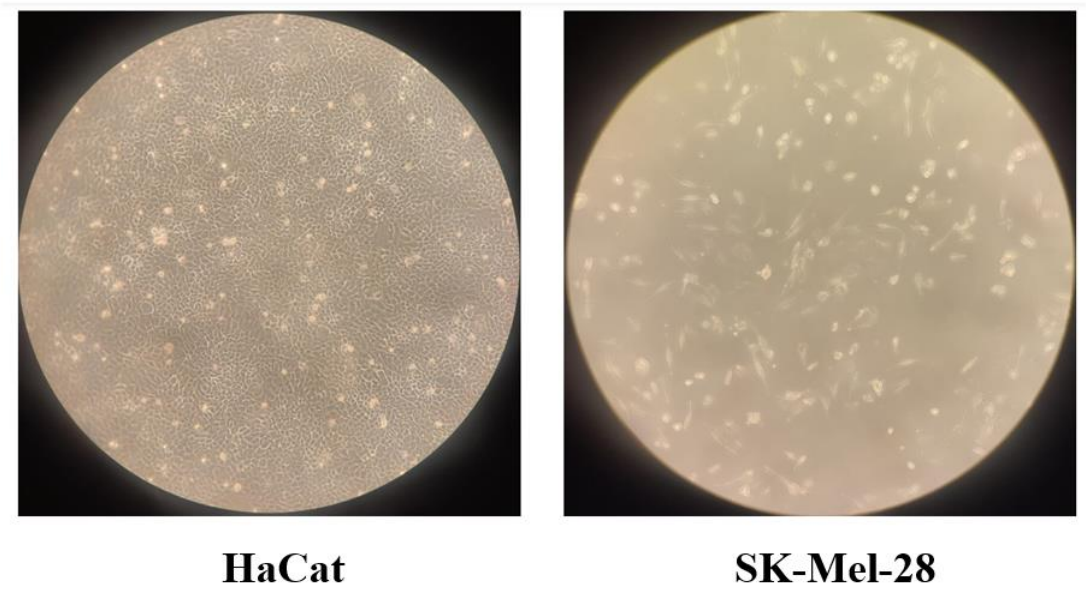

Figure 16: Phase-contrast microscopy (10x) images of HaCaT (left) and SK-MEL-28 (right) cells.

4.10.2 Crystal violet assay

Screening on cytotoxic concentrations of free Vismodegib on HaCaT and SK-Mel-28 cell lines after 48 hours of incubation was done with crystal violet assay.

Cell viability decreased in a dose-dependent manner for both cell lines. Significant reductions in viability were observed at concentrations above 60 μM, and at the highest concentration tested (360 μM), almost no viable cells remained. From the sigmoidal curve, the IC50 values were calculated as 89.56 μM for HaCaT cells and 86.26 μM for SK-Mel-28 cells, showing that both cell lines had similar sensitivity to the treatment. These results indicate that Vismodegib reduces the viability of both keratinocyte and melanoma cells at comparable levels (Figure 17).

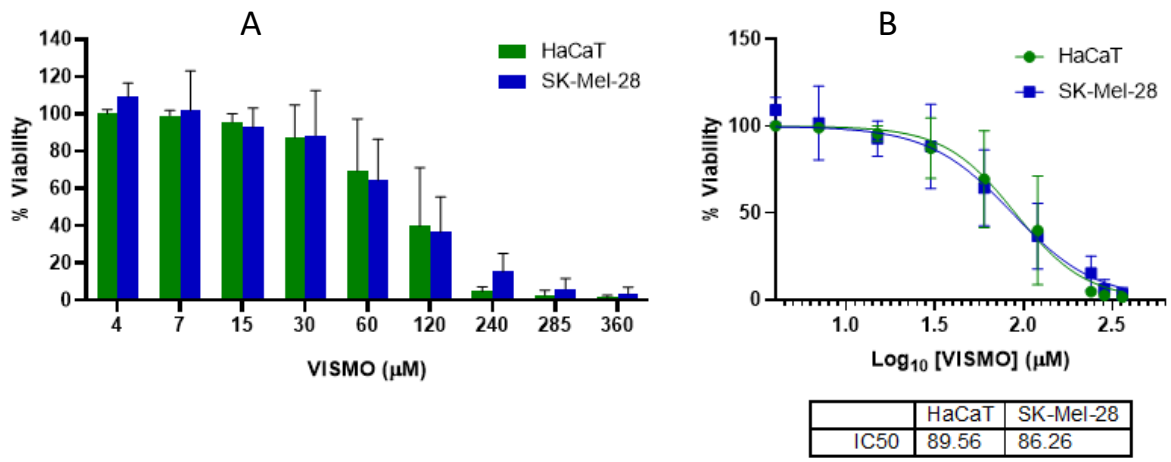

	HaCaT	SK-Mel-28
IC50	89.56	86.26

Figure 17: Cytotoxicity effects of free Vismodegib on both cell lines. Data are shown as the mean ± standard deviation of the percentage of cell viability versus drug concentration (A) and as a dose-response curve with the corresponding IC50 values (B).

4.10.3 Formulation cytotoxicity preliminary results

Screening on the effect of the cytotoxicity of the formulations after 48 hours of incubation was done with ATP-lite assay.

The results showed variability between the two cell lines, with the most pronounced effects observed at higher concentrations (Figure 18). In the HaCaT cell line, drug encapsulation has shown a reduction in cytotoxicity. Conversely, in the SK-Mel-28 cell line, VISMO-SIL exhibited higher cytotoxic effects compared to VISMO-SL at the highest tested concentration. Overall, the data indicated greater cytotoxicity of Vismodegib formulations on HaCaT cells compared to SK-Mel-28 cells. However, these results are based on a single experiment and do not align with the findings from the crystal violet assay of the free drug. Since this preliminary experiment was conducted only once, potential errors may have influenced the outcomes, highlighting the need for repetition to obtain more reliable and reproducible results.

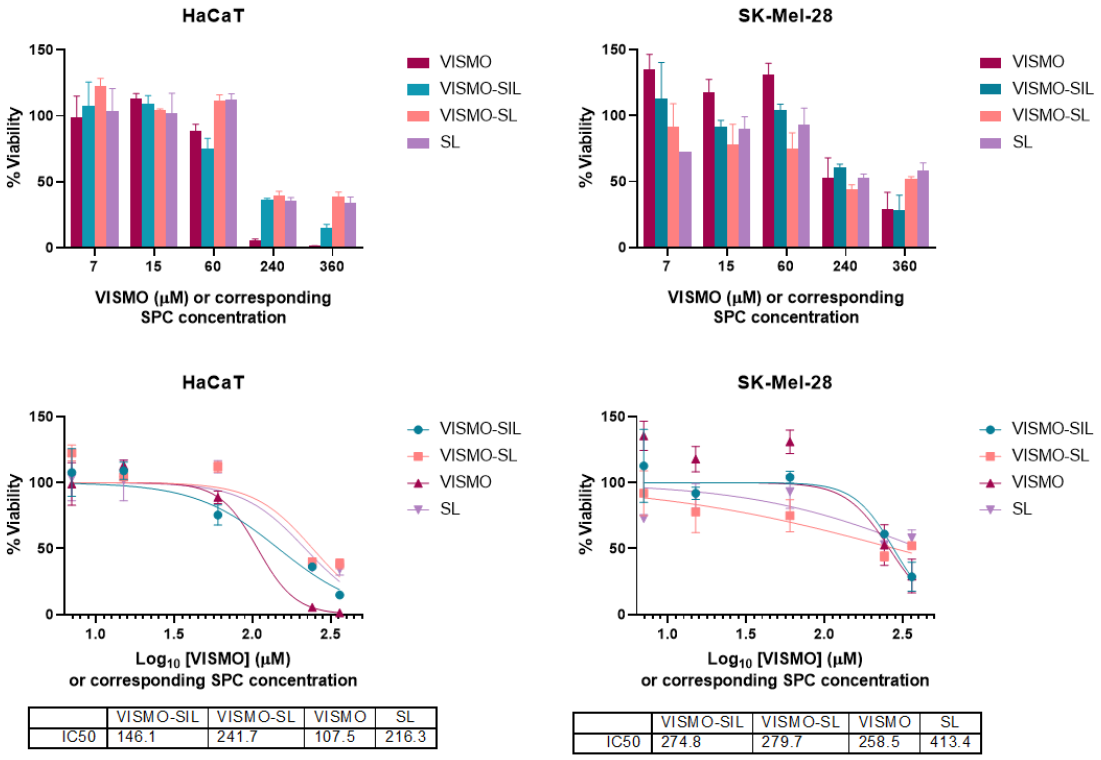

	VISMO-SIL	VISMO-SL	VISMO	SL
IC50	146.1	241.7	107.5	216.3

	VISMO-SIL	VISMO-SL	VISMO	SL
IC50	274.8	279.7	258.5	413.4

Figure 18: Comparative cytotoxicity of free Vismodegib and its encapsulated formulations (VISMO-SIL, VISMO-SL) and SL (diluted in the same concentration as VISMO-SL) on HaCaT and SK-Mel-28 cell lines. Top panels: bar graphs depicting the percentage of cell viability at different concentrations for each formulation and cell line. Bottom panels: dose-response curves the percentage of cell viability plotted against the log of Vismodegib concentrations, with corresponding IC50 values tabulated below.

5. Discussion

Skin cancer is among the most common cancers worldwide, with its prevalence continuing to rise despite increased awareness of risk factors, particularly excessive sun exposure. Skin cancer is broadly categorized into NMSC and melanoma skin cancer. Among NMSC, BCC is the most common, on the other hand generally, melanoma is the most aggressive form.

Advancements in skin cancer treatment have been limited over the past four decades, especially in comparison to other cancers. Conventional therapies, including immunotherapy, chemotherapy, radiotherapy, and their combinations, often yield suboptimal response rates, short median survival times, and significant toxicity. For early-stage NMSC, surgical approaches such as excision, and cryosurgery are standard. However, these treatments are invasive, frequently performed on sun-exposed areas like the face and scalp and may result in physical and emotional distress. Advanced skin cancers can cause severe local destruction, deformities, and even life-threatening conditions when vital structures are invaded.

One promising therapeutic target in skin cancer is the Hh signaling pathway, which plays a critical role in cancer progression and drug resistance. Aberrant activation of the Hh pathway is a hallmark of BCC and has been implicated in melanoma as well. Vismodegib, the first FDA-approved Hh pathway inhibitor, marked a breakthrough in the treatment of locally advanced or metastatic BCC. It offered an alternative to surgery and radiation by blocking the Hh pathway, effectively reducing tumor growth. However, Vismodegib is associated with side effects such as muscle spasms, alopecia, and dysgeusia, highlighting the need for safer and more effective therapeutic strategies.

Melanoma, while distinct in its pathophysiology, also demonstrates aberrant Hh pathway activation, making it a potential target for therapies like Vismodegib. Although more research is required to validate its effectiveness in melanoma, targeting this pathway could open new avenues for treating this aggressive cancer.

To enhance the precision and efficacy of cancer treatment, immunoliposomes offer a promising solution. These nanocarriers enable targeted drug delivery, minimizing damage to healthy tissues and reducing systemic toxicity. Combining Hh pathway inhibition with immune checkpoint blockade, such as targeting the PD-L1/PD-1 interaction, represents a novel and

potential synergistic approach. PD-L1/PD-1 interactions allow cancer cells to evade immune responses, and disrupting this pathway can reinvigorate the immune system to fight cancer.

This project aimed to develop an improved treatment strategy for inhibiting two critical pathways in cancer therapy, specifically targeting skin cancers such as BCC and melanoma. A key challenge in this process was optimizing the liposome formulation to efficiently encapsulate and deliver the hydrophobic drug. Due to the hydrophobic nature of the drug, it is essential for it to be incorporated within the liposomal bilayer, as it cannot be accommodated in the aqueous core. If the bilayer does not provide sufficient space, the drug may leak out. The initial formulation was prepared using the lab's standard protocol for Doxorubicin-loaded stealth liposomes, employing saturated lipids and cholesterol. However, this approach failed to encapsulate the drug, as the drug was entirely released during the process. To address this issue, the formulation strategy shifted to using unsaturated lipids in the bilayer to increase space in the hydrophobic bilayer for the drug. Despite this adjustment, a pellet was still observed at the bottom of the Eppendorf tube. Subsequent analysis of lipid concentration and incorporated drug mass revealed that the pellet consisted of the drug itself.

To tackle this problem, the first step was to replace saturated lipids with unsaturated ones, creating more space for the drug. In subsequent steps, the inclusion of cholesterol was avoided further to enhance the spaciousness of the bilayer, improving drug retention.

Additionally, by incorporating PEG during the preparation step, the liposomes were modified into "stealth" liposomes, which are designed to evade the immune system. This modification was intended to improve the liposomes' circulation time and half-life, thus enhancing their stability and retention within the bloodstream for prolonged therapeutic activity. Among all the nine formulations tested, which varied in lipid components and drug incorporation mass, "Formulation 8" prepared with unsaturated lipids, without cholesterol, and with an optimized amount of drug for the incorporation step, emerged as the best formulation, demonstrating the most favorable characteristics for effective drug delivery. Additionally, no pellet was observed at the bottom of the Eppendorf tube during preparation, indicating uniform incorporation of the drug within the liposomes and the absence of precipitation.

Once the final optimized formulation was obtained, two additional batches were prepared to evaluate the stability of the formulation over time. This stability study was conducted over a two-month period. As shown in the results, the formulation demonstrated good stability, with the z-average size consistently around 100 nm and a PDI consistently below 0.1. Another

important factor considered in the stability assessment was the retention of the incorporated drug. It was crucial to ensure that the drug remained encapsulated within the liposomes and did not escape over time. Although some minor loss of the drug was observed, the majority of the drug remained effectively retained within the liposomes, as confirmed by HPLC quantification.

After confirming the stability of the optimized formulation, the next step involved examining the morphology of the liposomes using TEM. The images revealed that the liposomes were uniformly rounded, further validating their size homogeneity and suitability for drug delivery. Encouraged by these results, the formulation was advanced to the next phase—transforming them into immunoliposomes.

To achieve this, the antibody Atezolizumab, which blocks the PD-L1 and disrupts PD-L1/PD-1 interactions to prevent immune suppression, was chosen. The Fab' fragment of the antibody was successfully purified and then PEGylated. The PEGylation of the Fab' was obtained by the reaction between the free thiol groups of Fab' and the commercial mal-PEG_{5kDa}-DSPE that yielded the formation of a thioether bond (thiol-Michael addition) between the maleimide group (mal) of PEG.Moreover, the DSPE moiety will allow the interaction of the conjugate with the surface of liposomes. To turn the VISMO-SL to VISMO-SIL these PEGylated Fab's were inserted into the liposome bilayer by post-insertion. To prevent any residual maleimide groups from reacting or interfering in subsequent steps or during *in vitro* experiments, they were inactivated by reaction with thioglycolic acid, which effectively blocks the free maleimide groups. However, upon disrupting the liposomes for quantification with HPLC, after the post-insertion step, it was discovered that nearly all of the drug had leaked out. It was hypothesized that the elevated post-insertion temperature (60 °C), which exceeded the lipid melting temperature, may have caused the leakage of the drug. To address this issue, the post-insertion was repeated at lower temperatures of 25 °C and 40 °C, with extended incubation times of 1, 24, and 48 hours to compensate for the reduced reaction kinetics. Despite these modifications, quantification revealed that the drug was still undetectable within the liposomes, confirming that temperature was not the primary factor responsible for drug leakage. This unexpected finding highlighted the need for further investigation into the interaction between the post-insertion process, liposomal stability, and drug leakage.

To overcome the challenges posed by drug leakage, alternative approaches were explored, as detailed in section 3.2.14.1. Through various hypotheses and experiments, it was eventually determined that the issue arose when additional components were inserted into the bilayer of the already-formed liposomes. This insertion process appeared to occupy some spaces in the

bilayer and allow the drug to escape. Conversely, when no components were inserted into the bilayer and only Fab' conjugation was performed, the drug remained incorporated within the liposomes. Interestingly, although the quantification results showed a reduction in the encapsulated drug, no pellet was observed at the bottom of the Eppendorf tubes after the post-insertion methods, unlike in earlier formulations. Since all the post-insertion processes involve additional PEG components that may have led to the formation of micelles, the escaped drug could partition into these micelles, explaining the absence of a visible pellet. On the contrary, in the approach that involved only the conjugation of Fab' without post-insertion, the drug mass incorporated in VISMO-SIL remained the same as in VISMO-SL.

This last approach was previously optimized with Trastuzumab's Fab'. For each experiment, the purification of the Fab' fragment from the whole antibody was essential, and the quality of the purification process was assessed using SDS-PAGE. To detect even low concentrations of proteins and ensure the presence of specific components, multiple staining techniques were employed, including iodine staining for PEG detection, coomassie staining for protein detection, and silver staining for enhanced sensitivity to detect even very low amounts of the protein.

Silver staining, while highly sensitive, posed significant challenges during its use. In the final step, adding the developer solution often caused the molecular weight marker to darken too quickly, obscuring the protein bands before they were adequately visualized. Additionally, liposomes did not migrate well in the gel, further complicating the analysis.

To address these issues, the molecular weight marker was diluted, which slowed its staining process and delayed its development. This adjustment allowed sufficient time for the protein bands to fully develop and become clearly visible. For the liposomes, various concentrations were tested to minimize interference with protein migration and optimize their behavior in the gel.

These improvements enhanced the accuracy and reproducibility of the staining process, enabling reliable detection of the Fab' and associated components.

Furthermore, TEM analysis following this step confirmed that the liposomes maintained a uniform and well-defined morphology. Notably, the comparison between VISMO-SL and VISMO-SIL revealed a slight increase in size, attributed to the presence of AB. Additionally, the zeta potential showed a marginal increase, becoming more negative.

For the *in vitro* studies, two cell lines were utilized: HaCaT, representing human keratinocytes, and SK-MEL-28, a human melanoma cell line. These were selected to evaluate the effects of liposomal formulation and the free drug in a tumoral and non-tumoral cell line. Drug cytotoxicity was assessed preliminarily using the crystal violet assay, which demonstrated that vismodegib exhibited cytotoxic effects within the concentration range that was successfully incorporated into the liposomal formulation. Furthermore, VISMO-SIL, VISMO-SL, SL, and the free drug cytotoxicity were also assessed with ATP-lite assay but as a preliminary test. The results indicated that for the HaCaT, the non-tumor cell line, the free drug was more toxic than the formulations, so the encapsulation decreased its cytotoxicity, while for the SK-Mel-28, the melanoma cell line, VISMO-SIL showed better cytotoxicity than the VISMO-SL in higher concentration, as expected, and similar than the free Vismodegib. However, this test was conducted only once as a preliminary study, and various potential errors might have influenced the outcome. Further repetitions and investigations will be conducted to validate these findings and reduce the variability in results.

In conclusion, the main objective of this study, which was to identify the optimal formulation for delivering Vismodegib into PD-L1-targeted liposomes, was successfully achieved. Preliminary *in-vitro* results suggest its potential for effective cancer treatment, showing enhanced efficacy against tumor cells in the presence of Fab', while maintaining similar performance to the free drug and reducing its cytotoxicity on non-tumor cells. However, these findings are based on a single trial, and further testing is necessary to obtain more reliable and reproducible data.

Targeting both the PD-L1/PD-1 interaction and the Hh signaling pathway offers a promising combined therapeutic strategy for skin cancers such as BCC and melanoma. However, since both pathways are also involved in other types of cancer, this formulation could potentially be repurposed in the future for targeted therapy with Vismodegib as well as immune checkpoint blockade using Atezolizumab’s Fab'. Additionally, given the hydrophobic nature of Vismodegib, exploring alternative delivery systems, such as solid lipid nanoparticles, can be beneficial. These systems may offer more space for incorporating hydrophobic drugs, potentially improving drug loading capacity and enhancing cytotoxic effects, as well as they can also be targeted. Moreover, *in vivo s*tudies are needed in the future to assess the antitumor efficacy.

References

1. American Cancer Society. (2014). *Cancer facts & figures 2014*. American Cancer Society. https://www.cancer.org/research/cancer-facts-statistics/all-cancer-facts-figures/cancer-facts-figures-2014.html

2. Hassanpour, S. H., & Dehghani, M. (2017). Review of cancer from perspective of molecular. *Journal of cancer research and practice*, *4*(4), 127-129.

3. National Cancer Institute. (n.d.). *Cancer*. National Cancer Institute. https://www.cancer.gov/publications/dictionaries/cancer-terms/def/cancer

4. National Cancer Institute. (2021). *The definition of cancer*. National Cancer Institute. https://www.cancer.gov/publications/dictionaries/cancer-terms/def/cancer

5. National Cancer Institute. (n.d.). *What is cancer*. National Cancer Institute. https://www.cancer.gov/about-cancer/understanding/what-is-cancer

6. Hofmann, E., Schwarz, A., Fink, J., Kamolz, L. P., & Kotzbeck, P. (2023). Modelling the complexity of human skin in vitro. *Biomedicines*, *11*(3), 794.

7. Reihsner, R., Balogh, B., & Menzel, E. J. (1995). Two-dimensional elastic properties of human skin in terms of an incremental model at the in vivo configuration. *Medical engineering & physics*, *17*(4), 304-313.

8. ong, R., Geyer, S., Weninger, W., Guimberteau, J. C., & Wong, J. K. (2016). The dynamic anatomy and patterning of skin. *Experimental dermatology*, *25*(2), 92-98.

9. Ashraf, R., Afzal, S., Rehman, A. U., Gul, S., Baber, J., Bakhtyar, M., ... & Maqsood, M. (2020). Region-of-interest based transfer learning assisted framework for skin cancer detection. *IEEE Access*, *8*, 147858-147871.

10. Byrd, A. L., Belkaid, Y., & Segre, J. A. (2018). The human skin microbiome. *Nature Reviews Microbiology*, *16*(3), 143-155.

11. Elgamal M. Automatic Skin Cancer Images Classification. International Journal of Advanced Computer Science and Applications. 2013;4(3).

12. National Cancer Institute. (n.d.). *Skin cancer prevention (PDQ®) – Patient version*. National Cancer Institute. https://www.cancer.gov/types/skin/patient/skin-prevention-pdq

13. Mayo Clinic. (n.d.). *Skin cancer*. Mayo Clinic. https://www.mayoclinic.org/diseases - conditions/skin-cancer/symptoms-causes/syc-20377605

14. Guy Jr, G. P., Machlin, S. R., Ekwueme, D. U., & Yabroff, K. R. (2015). Prevalence and costs of skin cancer treatment in the US, 2002− 2006 and 2007− 2011. *American journal of preventive medicine*, *48*(2), 183-187.

15. Green, A. (1992). Changing patterns in incidence of non-melanoma skin cancer. *Epithelial cell biology*, *1*(1), 47-51.

16. National Cancer Institute. (n.d.). *Skin cancer treatment (PDQ®) – Health professional version*. National Cancer Institute. https://www.cancer.gov/types/skin/hp/skin-treatment-pdq

17. WebMD. (n.d.). *Skin cancer: An overview*. WebMD. https://www.webmd.com/melanoma-skin-cancer/skin-cancer

18. Healthline. (2023). *Differences between basal cell carcinoma and melanoma*. Healthline. https://www.healthline.com/health/skin-cancer/basal-cell-carcinoma-vs-melanoma

19. Medical News Today. (2023). *What to know about melanoma vs. skin cancer*. Medical News Today. https://www.medicalnewstoday.com/articles/melanoma-vs-skin-cancer

20. MacKie, R. M., Hauschild, A., & Eggermont, A. M. M. (2009). Epidemiology of invasive cutaneous melanoma. *Annals of Oncology*, *20*, vi1-vi7.

21. Briatico, G., Mancuso, P., Argenziano, G., Longo, C., Mangone, L., Moscarella, E., ... & Pampena, R. (2022). Trends in cutaneous melanoma mortality in Italy from 1982 to 2016.

22. Hasan, N., Nadaf, A., Imran, M., Jiba, U., Sheikh, A., Almalki, W. H., ... & Ahmad, F. J. (2023). Skin cancer: understanding the journey of transformation from conventional to advanced treatment approaches. *Molecular cancer*, *22*(1), 168.

23. Li, X., Lovell, J. F., Yoon, J., & Chen, X. (2020). Clinical development and potential of photothermal and photodynamic therapies for cancer. *Nature reviews Clinical oncology*, *17*(11), 657-674.

24. Chandra, J., Hasan, N., Nasir, N., Wahab, S., Thanikachalam, P. V., Sahebkar, A., ... & Kesharwani, P. (2023). Nanotechnology-empowered strategies in treatment of skin cancer. *Environmental Research*, *235*, 116649.

25. Park, J. W., Benz, C. C., & Martin, F. J. (2004, December). Future directions of liposome-and immunoliposome-based cancer therapeutics. In *Seminars in oncology* (Vol. 31, pp. 196-205). WB Saunders.

26. Suri, S. S., Fenniri, H., & Singh, B. (2007). Nanotechnology-based drug delivery systems. *Journal of occupational medicine and toxicology*, *2*, 1-6.

27. Düzgüneş, N., & Gregoriadis, G. (2005). Introduction: the origins of liposomes: Alec Bangham at Babraham. In *Methods in Enzymology* (Vol. 391, pp. 1-3). Academic Press.

28. Bozzuto, G., & Molinari, A. (2015). Liposomes as nanomedical devices. *International journal of nanomedicine*, 975-999.

29. Science Photo Library. (n.d.). *Phospholipid structures [Illustration]*. Science Photo Library. https://www.sciencephoto.com/media/1383052/view/phospholipid-structures-illustration

30. Li, J., Wang, X., Zhang, T., Wang, C., Huang, Z., Luo, X., & Deng, Y. (2015). A review on phospholipids and their main applications in drug delivery systems. *Asian journal of pharmaceutical sciences*, *10*(2), 81-98.

31. Allen, T. M. (1997). Liposomes: opportunities in drug delivery. *Drugs*, *54*(Suppl 4), 8-14.

32. Castañeda-Reyes, E. D., Perea-Flores, M. D. J., Davila-Ortiz, G., Lee, Y., & Gonzalez de Mejia, E. (2020). Development, characterization and use of liposomes as amphipathic transporters of bioactive compounds for melanoma treatment and reduction of skin inflammation: A review. *International journal of Nanomedicine*, 7627-7650.

33. Maherani, B., Arab-Tehrany, E., R Mozafari, M., Gaiani, C., & Linder, M. (2011). Liposomes: a review of manufacturing techniques and targeting strategies. *Current nanoscience*, *7*(3), 436-452.

34. Shi, N. Q., & Qi, X. R. (2021). Preparation of drug liposomes by reverse-phase evaporation. *Liposome-Based Drug Delivery Systems*, 37-46.

35. Akbarzadeh, A., Rezaei-Sadabady, R., Davaran, S., Joo, S. W., Zarghami, N., Hanifehpour, Y., ... & Nejati-Koshki, K. (2013). Liposome: classification, preparation, and applications. *Nanoscale research letters*, *8*, 1-9.

36. Du Plessis, J., Ramachandran, C., Weiner, N., & Müller, D. G. (1996). The influence of lipid composition and lamellarity of liposomes on the physical stability of liposomes upon storage. *International journal of pharmaceutics*, *127*(2), 273-278.

37. Torchilin, V. P. (2005). Recent advances with liposomes as pharmaceutical carriers. *Nature reviews Drug discovery*, *4*(2), 145-160.

38. Bozzuto, G., & Molinari, A. (2015). Liposomes as nanomedical devices. *International journal of nanomedicine*, 975-999.

39. Weissig, V. (2017). Liposomes came first: The early history of liposomology. *Liposomes: Methods and Protocols*, 1-15.

40. Milla, P., Dosio, F., & Cattel, L. (2012). PEGylation of proteins and liposomes: a powerful and flexible strategy to improve the drug delivery. *Current drug metabolism*, *13*(1), 105-119.

41. Roberts, M. J., Bentley, M. D., & Harris, J. M. (2002). Chemistry for peptide and protein PEGylation. *Advanced drug delivery reviews*, *54*(4), 459-476.

42. Subhan, M. A., Yalamarty, S. S. K., Filipczak, N., Parveen, F., & Torchilin, V. P. (2021). Recent advances in tumor targeting via EPR effect for cancer treatment. *Journal of personalized medicine*, *11*(6), 571.

43. Song, Y. Y., Yuan, Y., Shi, X., & Che, Y. Y. (2020). Improved drug delivery and anti-tumor efficacy of combinatorial liposomal formulation of genistein and plumbagin by targeting Glut1 and Akt3 proteins in mice bearing prostate tumor. *Colloids and Surfaces B: Biointerfaces*, *190*, 110966.

44. Manjappa, A. S., Chaudhari, K. R., Venkataraju, M. P., Dantuluri, P., Nanda, B., Sidda, C., ... & Murthy, R. S. R. (2011). Antibody derivatization and conjugation strategies: application in preparation of stealth immunoliposome to target chemotherapeutics to tumor. *Journal of Controlled Release*, *150*(1), 2-22.

45. Elkhoury, K., Koçak, P., Kang, A., Arab-Tehrany, E., Ellis Ward, J., & Shin, S. R. (2020). Engineering smart targeting nanovesicles and their combination with hydrogels for controlled drug delivery. *Pharmaceutics*, *12*(9), 849.

46. Wang, W., Singh, S., Zeng, D. L., King, K., & Nema, S. (2007). Antibody structure, instability, and formulation. *Journal of pharmaceutical sciences*, *96*(1), 1-26.

47. Martsev, S. P., Tsybovsky, Y. I., Stremovskiy, O. A., Odintsov, S. G., Balandin, T. G., Arosio, P., ... & Deyev, S. M. (2004). Fusion of the antiferritin antibody VL domain to barnase results in enhanced solubility and altered pH stability. *Protein Engineering Design and Selection*, *17*(1), 85-93.

48. Xenaki, K. T., Oliveira, S., & van Bergen En Henegouwen, P. M. (2017). Antibody or antibody fragments: implications for molecular imaging and targeted therapy of solid tumors. *Frontiers in immunology*, *8*, 1287.

49. Andrew, S. M., & Titus, J. A. (1997). Fragmentation of immunoglobulin G. *Current protocols in immunology*, *21*(1), 2-8.

50. Dozier, J. K., & Distefano, M. D. (2015). Site-specific PEGylation of therapeutic proteins. *International journal of molecular sciences*, *16*(10), 25831-25864.

51. National Cancer Institute. (2024). *Atezolizumab*. National Cancer Institute. https://www.cancer.gov/about-cancer/treatment/drugs/atezolizumab

52. DrugBank Online. (n.d.). *Atezolizumab: Uses, interactions, mechanism of action*. DrugBank Online. https://go.drugbank.com/drugs/DB12047

53. Zou, W., Wolchok, J. D., & Chen, L. (2016). PD-L1 (B7-H1) and PD-1 pathway blockade for cancer therapy: Mechanisms, response biomarkers, and combinations. *Science translational medicine*, *8*(328), 328rv4-328rv4.

54. Sun, C., Mezzadra, R., & Schumacher, T. N. (2018). Regulation and function of the PD-L1 checkpoint. *Immunity*, *48*(3), 434-452.

55. Zak, K. M., Grudnik, P., Guzik, K., Zieba, B. J., Musielak, B., Dömling, A., ... & Holak, T. A. (2016). Structural basis for small molecule targeting of the programmed death ligand 1 (PD-L1). *Oncotarget*, *7*(21), 30323.

56. Naidoo, J., Page, D. B., Li, B. T., Connell, L. C., Schindler, K., Lacouture, M. E., ... & Wolchok, J. D. (2015). Toxicities of the anti-PD-1 and anti-PD-L1 immune checkpoint antibodies. *Annals of Oncology*, *26*(12), 2375-2391.

57. Stonesifer, C. J., Djavid, A. R., Grimes, J. M., Khaleel, A. E., Soliman, Y. S., Maisel-Campbell, A., ... & Carvajal, R. D. (2021). Immune checkpoint inhibition in non-melanoma skin Cancer: a review of current evidence. *Frontiers in oncology*, *11*, 734354.

58. Spranger, S., Spaapen, R. M., Zha, Y., Williams, J., Meng, Y., Ha, T. T., & Gajewski, T. F. (2013). Up-regulation of PD-L1, IDO, and Tregs in the melanoma tumor microenvironment is driven by CD8+ T cells. *Science translational medicine*, *5*(200), 200ra116-200ra116.

59. Barot, S., Patel, H., Yadav, A., & Ban, I. (2023). Recent advancement in targeted therapy and role of emerging technologies to treat cancer. *Medical Oncology*, *40*(11), 324.

60. Rudin, C. M., Hann, C. L., Laterra, J., Yauch, R. L., Callahan, C. A., Fu, L., ... & Low, J. A. (2009). Treatment of medulloblastoma with hedgehog pathway inhibitor GDC-0449. *New England Journal of Medicine*, *361*(12), 1173-1178.

61. Sandhiya, S., Melvin, G., Kumar, S. S., & Dkhar, S. A. (2013). The dawn of hedgehog inhibitors: Vismodegib. *Journal of Pharmacology and Pharmacotherapeutics*, *4*(1), 4-7.

62. Dlugosz, A., Agrawal, S., & Kirkpatrick, P. (2012). Vismodegib. *Nature reviews Drug discovery*, *11*(6).

63. Genentech. (n.d.). *Erivedge*. Genentech. https://www.gene.com/products/early-stage-products/erivedge

64. Sekulic, A., Migden, M. R., Oro, A. E., Dirix, L., Lewis, K. D., Hainsworth, J. D., ... & Hauschild, A. (2012). Efficacy and safety of vismodegib in advanced basal-cell carcinoma. *New England Journal of Medicine*, *366*(23), 2171-2179.

65. Zhang, H., Sun, Z., Liu, Z., & Song, C. (2018). Overcoming the emerging drug resistance of smoothened: an overview of small-molecule SMO antagonists with antiresistance activity. *Future Medicinal Chemistry*, *10*(24), 2855-2875.

66. U.S. Food and Drug Administration. (2020). *FDA approves atezolizumab for BRAF V600 unresectable or metastatic melanoma*. U.S. Food and Drug Administration. https://www.fda.gov/news-events/press-announcements/fda-approves-atezolizumab-braf-v600-unresectable-or-metastatic-melanoma

67. Zhang, Y., Yang, M., Portney, N. G., Cui, D., Budak, G., Ozbay, E., ... & Ozkan, C. S. (2008). Zeta potential: a surface electrical characteristic to probe the interaction of nanoparticles with normal and cancer human breast epithelial cells. *Biomedical microdevices*, *10*, 321-328.

68. Prima, G.D., Librizzi, F., & Carrotta, R. (2020). Light scattering as an easy tool to measure vesicles weight concentration. *Membranes* , *10* (9), 222.

69. Calienni, M. N., Febres-Molina, C., Llovera, R. E., Zevallos-Delgado, C., Tuttolomondo, M. E., Paolino, D., ... & Montanari, J. (2019). Nanoformulation for potential topical delivery of Vismodegib in skin cancer treatment. *International Journal of Pharmaceutics*, *565*, 108-122.

70. Olson, B. J. (2016). Assays for determination of protein concentration. *Current Protocols in Pharmacology*, *73*(1), A-3A.

71. Bhuyan. (2023). *Biuret test*. Chemistry Learner. https://www.chemistrylearner.com/biuret- test.html

72. Gallagher, S. R. (2012). SDS-polyacrylamide gel electrophoresis (SDS-PAGE). *Current Protocols Essential Laboratory Techniques*, *6*(1), 7-3.

73. Canato, E. (2018). Development of novel super stealth immunoliposomes for anticancer drug delivery.

74. Liang, G., Liu, M., Wang, Q., Shen, Y., Mei, H., Li, D., & Liu, W. (2017). Itraconazole exerts its anti-melanoma effect by suppressing Hedgehog, Wnt, and PI3K/mTOR signaling pathways. *Oncotarget*, *8*(17), 28510.

75. Liu, H., Jian, Q., Xue, K., Ma, C., Xie, F., Wang, R., ... & Li, C. (2014). The MEK/ERK signalling cascade is required for sonic hedgehog signalling pathway-mediated enhancement of proliferation and inhibition of apoptosis in normal keratinocytes. *Experimental dermatology*, *23*(12), 896-901.